

REPORT DOCUMENTATION PAGE		Form Approved OMB NO. 0704-0188	
Public Reporting Burden for this collection of information is estimated to average 1 hour per response, including the time for reviewing instructions, searching existing data sources, gathering and maintaining the data needed, and completing and reviewing the collection of information. Send comment regarding this burden estimate or any other aspect of this collection of information, including suggestions for reducing this burden, to Washington Headquarters Services, Directorate for Information Operations and Reports, 1215 Jefferson Davis Highway, Suite 1204, Arlington VA, 22202-4302, and to the Office of Management and Budget, Paperwork Reduction Project (0704-0188), Washington DC 20503			
1. AGENCY USE ONLY (Leave Blank)		2. REPORT DATE:	
		3. REPORT TYPE AND DATES COVERED Final Report 15-Aug-2003 - 31-Dec-2005	
4. TITLE AND SUBTITLE Wavelet-Based Blind Superresolution from Video Sequence and in MRI		5. FUNDING NUMBERS DAAD190310261	
6. AUTHORS Professor N. K. Bose		8. PERFORMING ORGANIZATION REPORT NUMBER	
7. PERFORMING ORGANIZATION NAMES AND ADDRESSES Pennsylvania State University Office of Sponsored Programs 110 Technology Center, 200 Innovation Blvd. University Park, PA 16802 -			
9. SPONSORING/MONITORING AGENCY NAME(S) AND ADDRESS(ES) U.S. Army Research Office P.O. Box 12211 Research Triangle Park, NC 27709-2211		10. SPONSORING / MONITORING AGENCY REPORT NUMBER 44250-CI.2	
11. SUPPLEMENTARY NOTES The views, opinions and/or findings contained in this report are those of the author(s) and should not be construed as an official Department of the Army position, policy or decision, unless so designated by other documentation.			
12. DISTRIBUTION AVAILABILITY STATEMENT Approved for Public Release; Distribution Unlimited		12b. DISTRIBUTION CODE	
13. ABSTRACT (Maximum 200 words) The abstract is below since many authors do not follow the 200 word limit			
14. SUBJECT TERMS blind deconvolution, blur support estimation, multiframe deblurring, image sequence superresolution, moving least-squares		15. NUMBER OF PAGES Unknown due to possible attachments	
		16. PRICE CODE	
17. SECURITY CLASSIFICATION OF REPORT UNCLASSIFIED	18. SECURITY CLASSIFICATION ON THIS PAGE UNCLASSIFIED	19. SECURITY CLASSIFICATION OF ABSTRACT UNCLASSIFIED	20. LIMITATION OF ABSTRACT UL

## Report Title

### Wavelet-Based Blind Superresolution from Video Sequence

#### ABSTRACT

The first contribution of this research is the development of a mathematical framework for deployment of second-generation wavelets for image superresolution. Second, the Biggs-Andrews multichannel iterative blind deconvolution (IBD) algorithm is modified to include the blur support estimation module. Then the asymmetry factor for the Richardson-Lucy update-based IBD algorithm is calculated. Simulations conducted on real-world and synthetic images confirm the importance of accurate support estimation in the blind superresolution problem. The effect of the threshold level on reconstructed image quality in second-generation wavelet superresolution is investigated and a measure based on the singular values of the image matrix is employed as a reliable gauge of visual image quality. A discrete implementation of the moving least squares (MLS) is made on images and the effect of choice of the two dependent parameters, scale and order, on noise filtering and reduction of blur introduced during the MLS process is studied. Finally, the role of brushlets in textured image denoising and segmentation is investigated and plans made for future research in miniaturized computational imaging systems for superresolution with increased field of view.

---

#### **List of papers submitted or published that acknowledge ARO support during this reporting period. List the papers, including journal references, in the following categories:**

##### **(a) Papers published in peer-reviewed journals (N/A for none)**

N. K. Bose, S. Lertrattanapanich and M. B. Chappalli, Superresolution with Second Generation Wavelets, Signal Processing, Image Communication, 19 (5), pp.387-391, 2004.

N. K. Bose and M. B. Chappalli, A Second Generation Wavelet Framework for Superresolution with Noise Filtering, International J. on Imaging Science and Technology (Special Issue on High Resolution Image Reconstruction), Vol. 14, No. 2, pp. 84-89, 2004.

N. A. Ahuja and N. K. Bose, Spatiotemporal-Bandwidth Product of m-Dimensional signals, IEEE Signal Processing Letters, Vol. 12, No. 2, pp. 123-125, Feb 2005

Chih-Chung Yang and N. K. Bose, Landmine Detection and Classification With Complex-Valued Hybrid Neural Network Using Scattering Parameters Dataset, IEEE Transactions on Neural Networks, vol. 16, no. 3, May 2005, pp. 743-753.

Mahesh B. Chappalli and N. K. Bose, Simultaneous Noise Filtering and Super-Resolution With Second-Generation Wavelets, IEEE Signal Processing Letters, Vol. 12, No. 11, pp. 772-775, Nov 2005.

N. Ahuja, S. Lertrattanapanich and N. K. Bose, "Properties determining choice of mother wavelet," IEE Proceedings on Vision, Image and Signal Processing, Volume 152, Issue 5, October 2005, pp. 659 - 664.

Chih-Chung Yang and N.K. Bose, Generating fuzzy membership function with self-organizing feature map, Pattern Recognition Letters 27 (2006) pp. 356-365.

N. K. Bose and Nilesh A. Ahuja, Superresolution and Noise Filtering Using Moving Least Squares, accepted for publication in IEEE Transactions On Image Processing.

M. B. Chappalli and N. K. Bose, Enhanced Biggs-Andrews asymmetric iterative blind deconvolution, accepted for publication in Multidimensional Systems and Signal Processing.

N. K. Bose, Michael K. Ng and Andy C. Yau, A fast algorithm for image super-resolution from blurred observations, accepted for publication in EURASIP Journal on Applied Signal Processing

Number of Papers published in peer-reviewed journals: 10.00

---

**(b) Papers published in non-peer-reviewed journals or in conference proceedings (N/A for none)**

N. K. Bose, M. K. Ng, A. C. Yau, Super-Resolution Image Restoration from Blurred Observations, Proceedings of International Symposium on Circuits and Systems (ISCAS 2005), Kobe, Japan pp. 6296-6299, May 2005.

Number of Papers published in non peer-reviewed journals: 1.00

---

**(c) Papers presented at meetings, but not published in conference proceedings (N/A for none)**

N. K. Bose, Blind Superresolution Research: PSF Support Estimation, Invited ARDA Workshop Participant, ORNL, TN, February 2005

N. K. Bose, Generalized Sampling Theorem for BL Signals, Invited ARDA Workshop Participant, ORNL, TN, June 2005

N. K. Bose, Critical Issues for PERIODIC, Invited ARDA Workshop Participant, ORNL, TN, October 2005

N. K. Bose, Latest Results on Superresolution, Akita Prefectural University, Honjo, Japan, August 2005

N. K. Bose, Iterative Blind Second Generation Wavelet Superresolution and the Role of Moving Least Squares, International Conference on Super-Resolution Imaging, August 29-September 1, 2005, University of HongKong, HongKong.

Number of Papers not Published: 5.00

---

**(d) Manuscripts**

Nilesh A. Ahuja and N. K. Bose, "Multidimensional Generalized Sampling Theorem for Wavelet Based Image Superresolution," International Conference on Image Processing, Atlanta, Georgia, 2006.

Andy C.Yau, N. K. Bose,and Michael K. Ng, "An Efficient Algorithm for Superresolution in Medium Field Imaging," Multidimensional Systems and Signal Processing, Revision completed on March 22, 2006.

Number of Manuscripts: 2.00

---

**Number of Inventions:**

---

**Graduate Students**

<u>NAME</u>	<u>PERCENT</u>	<u>SUPPORTED</u>	
Mahesh B. Chappalli	0.50	No	
Nilesh A. Ahuja	0.50	No	
Andy Yau	0.25	No	
Chih-Chung Yang	0.25	No	
Dinesh Somasundaram Iyer	0.10	No	
<b>FTE Equivalent:</b>	<b>1.60</b>		
<b>Total Number:</b>	<b>5</b>		

**Names of Post Doctorates**

<u>NAME</u>	<u>PERCENT</u>	<u>SUPPORTED</u>
<b>FTE Equivalent:</b>		
<b>Total Number:</b>		

---

### Names of Faculty Supported

<u>NAME</u>	<u>PERCENT SUPPORTED</u>	National Academy Member
Nirmal K. Bose	0.25	No
<b>FTE Equivalent:</b>	<b>0.25</b>	
<b>Total Number:</b>	<b>1</b>	

---

### Names of Under Graduate students supported

<u>NAME</u>	<u>PERCENT SUPPORTED</u>	
Zachary Harmany		No
<b>FTE Equivalent:</b>		
<b>Total Number:</b>	<b>1</b>	

---

### Names of Personnel receiving masters degrees

<u>NAME</u>	
Dinesh Somasundaram Iyer	No
Kenneth Neiss	No
Sarah Lannes	No
Nilesh Ahuja	No
<b>Total Number:</b>	<b>4</b>

---

### Names of personnel receiving PHDs

<u>NAME</u>	
Mahesh B. Chappalli	No
Chih-Chung Yang	No
<b>Total Number:</b>	<b>2</b>

---

### Names of other research staff

<u>NAME</u>	<u>PERCENT SUPPORTED</u>
<b>FTE Equivalent:</b>	
<b>Total Number:</b>	

---

### Sub Contractors (DD882)

### Inventions (DD882)



# **Wavelet-Based Blind Superresolution from Video Sequence**

Army Research Office Grant DAAD 19-03-1-0261

Research was Sponsored by: **U. S. ARMY RESEARCH  
OFFICE**

**Research Triangle Park  
NC 27709-2211**

**Principal Investigator:**

**Dr. N. K. Bose**

**Director, The Spatial and Temporal Signal Processing Center**

**Department of Electrical Engineering**

**The Pennsylvania State University**

**University Park, PA 16802**

# Contents

<b>1</b>	<b>Foreword</b>	<b>1</b>
<b>2</b>	<b>Statement of the Problem Studied</b>	<b>1</b>
<b>3</b>	<b>Summary of the Most Important Results Obtained</b>	<b>2</b>
3.1	Optimal Choice of Threshold in Second Generation Wavelet Superresolution [2]	3
3.2	Iterative PSF Support Estimation for the Biggs-Andrews Iterative Blind Deconvolution algorithm [3] . . . . .	3
3.3	Moving Least Squares in Image Sequence Superresolution [4] . . . . .	4
<b>4</b>	<b>Appendix</b>	<b>4</b>

# 1 Foreword

Image superresolution refers to methods that increase spatial resolution by fusing information from a sequence of images, acquired in one or more of several possible ways. The high resolution filtered image is constructed from the aliased (undersampled) noisy and blurred frames with either subpixel shifts or the use of intentional blurring by designing lenses with different point spread functions.

A demand for higher resolution is seen in many fields including bio-medical imaging (for purposes like image-guided surgery and image-assisted medical diagnosis), entertainment (high definition television or HDTV), satellite and astronomical imaging, chemical and biological research (high resolution electron microscopy), military surveillance and remote sensing. Indeed, this demand, in many cases, exceeds the maximum resolution capability of current acquisition systems. In other words, the current state of image sensor technology acts as a limiting factor in acquisition. In various other cases, factors such as cost, physical attributes like size and weight, and quality, instead of technology, constrain the maximum resolution obtainable from the acquisition device. Yet another set of cases exist in which resolution is compromised due to the need for flexibility and robustness with respect to various environmental conditions, among others. In all such cases, the solution to the need for higher resolution necessitates the design of technological devices in the form of digital image processing algorithms to satisfy the demand for high quality and high resolution (HR) images and video.

## 2 Statement of the Problem Studied

Wavelet superresolution is a topic that was introduced only about five years back. Prior to this research, all approaches used only first generation wavelets without adequate attention to the choice of mother wavelets. Second generation scaling functions and wavelets differ from their first generation counterparts in the property that they are not necessarily translates and dilates of one function. This allows adaptation to more generic conditions (such as irregular samples, weights, surfaces etc.) while preserving some powerful and important properties



of FGWs such as time-frequency localization, multi-resolution analysis and the existence of fast transforms. This renders SGWs useful in many real-life problems and applications where FGWs cannot be readily applied. Since SGWs sacrifice the properties of translation and dilation, they cannot be constructed using Fourier transform based methods and instead rely on the lifting scheme, which is an entirely spatial domain construction technique.

The attribute ‘*blind*’ applied to the superresolution problem denotes the lack of information on the function(s) representing the blur in the system. Therefore, a HR reconstruction algorithm/method should include image registration, denoising and deblurring components in addition to the superresolution module.

This research presents new computationally efficient algorithms for superresolution which offer better performance than other current methods. Typically, the superresolution module is followed by a separate denoising module. But in the case of the superresolution algorithms presented in this research, this module is rendered unnecessary since denoising is achieved simultaneously with superresolution, and is hence implicit to the superresolution module. The final step involves a multi-frame blind deconvolution algorithm which results in a denoised and deblurred high resolution image. This research improves on the performance of a popular and effective blind deconvolution algorithms which extends directly to the multi-frame case.

### 3 Summary of the Most Important Results Obtained

The use of second generation wavelets (SGWs) to attain superresolution (from a captured sequence of low resolution noisy and blurred frames) with noise filtering has been shown to be possible without any assumption on grid (sampling lattice) structure. The mathematical framework developed [1] is based on nonseparable two-dimensional methods after demonstrating the feasibility in the separable case. The procedure allows the incorporation of the more general projective camera motion model into the framework, instead of only displacement and rotational models. The primary goal of achieving blind superresolution with blur support estimation has been realized. The results obtained proceed from a special but useful case of fast super-resolution under periodic boundary condition, derivation of an optimal

threshold to resolve the tradeoff between conflicting factors of satisfactory blur removal and noise reduction for a visually pleasing superresolved image, to, subsequently, multiframe blind superresolution and noise filtering with, importantly, the accurate estimation of blur support.

### **3.1 Optimal Choice of Threshold in Second Generation Wavelet Superresolution [2]**

Wavelet coefficient thresholding has been shown to be effective in reducing spatial domain noise in the second generation wavelet based super-resolution algorithm. At the same time, thresholding of wavelet coefficients increases the blurring in an image due to loss of high frequency information. Hence, the choice of threshold for noise reduction should be made in a manner so as to achieve an optimal trade-off between the desirable noise reduction and the undesirable blurring. In this research, the effect of the threshold level on reconstructed image quality has been investigated. In the presence of blurring in the input along with noise, the choice of threshold plays an important role in determining the visual quality of the generated high-resolution image. The unsuitability of PSNR as a measure of image quality is confirmed and a new measure based on the singular values of the image is employed. Optimal choice of the threshold for noise filtering has been coupled with adaptive neighborhoods for prediction, both of which improve the performance of the second generation wavelet superresolution (SGWSR) algorithms.

### **3.2 Iterative PSF Support Estimation for the Biggs-Andrews Iterative Blind Deconvolution algorithm [3]**

The issue of blur in blind multiframe superresolution has been handled, especially in conjunction with an accurate estimation of unknown blur support. The iterative multiframe blind deconvolution algorithm considered by Biggs-Andrews requires exact knowledge of the support of the PSF for optimal performance and this is a serious drawback. Thus, in a sense, it is not totally blind. A significant outcome of this research is the modification of the Biggs-Andrews algorithm so that it incorporates the important step of iterative point

spread function (PSF) support estimation.

### 3.3 Moving Least Squares in Image Sequence Superresolution [4]

The Moving Least Squares (MLS) method is a technique that is likely to have a place in the task of image sequence superresolution because of its ability to interpolate over a grid of irregularly spaced data points created by the undersampled, low-resolution, possibly blurred and noisy images. The basis functions chosen in approximation to get the interpolant are usually multivariate polynomials, and the highest total degree of the polynomial used is the order of approximation. A weighted least-squares estimation procedure is used to find the coefficients of the basis function. The weight function used is the Gaussian function.

## References

- [1] N. K. Bose and M. B. Chappalli, “A second generation wavelet framework for super-resolution with noise filtering”, *International J. on Imaging Science and Technology (Special Issue on High Resolution Image Reconstruction)*, vol. 14, no. 2, pp. 8489, 2004.
- [2] M. B. Chappalli and N. K. Bose, “Simultaneous noise filtering and superresolution with second-generation wavelets”, *IEEE Signal Processing Letters*, vol. 12, no. 11, pp. 772775, November 2005.
- [3] M. B. Chappalli and N. K. Bose, “Enhanced Biggs-Andrews asymmetric iterative blind deconvolution”, *Multidimensional Systems and Signal Processing*, accepted for publication, 2005.
- [4] N. K. Bose and Nilesch. A. Ahuja, “Superresolution and noise filtering using moving least squares”, *IEEE Transactions on Image Processing*, accepted for publication, 2005.

## 4 Appendix

Documents describing in detail the research results mentioned above are presented next.

# A Second-Generation Wavelet Framework for Super-Resolution with Noise Filtering

N. K. Bose, Mahesh B. Chappalli

Department of Electrical Engineering, The Spatial and Temporal Signal Processing Center, The Pennsylvania State University, University Park, PA 16802

Received 12 February 2004; accepted 31 March 2004

**ABSTRACT:** The use of second-generation wavelets to attain super-resolution with noise filtering is described for a captured sequence of low-resolution frames without any assumptions on grid (sampling lattice) structure. The approach is based on 2D methods. The procedure allows the incorporation of the more general projective camera motion model into the framework, instead of only displacement and rotational models. Several simulations that compare the implementations of the algorithm presented here with other related approaches help illustrate the suitability of SGWs (coupled with hard or soft thresholding) in the task of image sequence superresolution with simultaneous noise filtering. © 2004 Wiley Periodicals, Inc. *Int J Imaging Syst Technol*, 14, 84–89, 2004; Published online in Wiley InterScience (www.interscience.wiley.com). DOI 10.1002/ima.20011

**Key words:** image sequence super-resolution; second-generation wavelets; high-resolution reconstruction

## I. MOTIVATION AND INTRODUCTION

In this section the suitability of second-generation wavelets (SGWs) for image sequence super-resolution is justified to be the motivating factor behind the research described here. This is followed by background material, with primary emphasis on the conditions important in the attainment of super-resolution, like subpixel displacements between adjacent frames, because this requirement is also crucial to the procedure developed here.

**A. Motivation.** First-generation wavelets (FGWs) that are dilates and translates of a chosen mother wavelet imply a regular sampling of the data, are defined on infinite domains, and have difficulties in dealing with boundaries. At the boundary, where one runs out of data as in the case of a digital image frame with a finite number of pixels, zero padding, cyclic and acyclic extensions of data have been used in the past. Special basis functions (translates and dilates of a vector of scaling functions) (Windmolders et al., 2003) near the boundary such that all basis functions are defined over the finite extent array are possible to use, but still adaptations near the boundary will be required. Furthermore, image sequence super-resolution (high resolution) can be viewed in the context of the conversion of the high-resolution nonuniformly sampled raster (irregular grid or

nonuniform sampling lattice) generated from an acquired sequence of low-resolution frames to the desired uniformly sampled high-resolution grid. Second-generation wavelets (SGWs) can not only deal with bounded domains and arbitrary boundary conditions, but also irregular sampling intervals, which are at the heart of a sequence of low-resolution images from which image super-resolution is desired. FGWs have been used in image sequence super-resolution during the last three or four years (Bose and Lertrattanapanich, 2004; Nguyen and Milanfar, 2000).

SGWs replace dilations and translations with an entirely spatial domain lifting scheme (Sweldens, 1998) based on the operations of splitting, prediction, and updating. They are suitable for use in multidimensions. In the lifting scheme, the forward transform is implementable with low storage and computational time costs; the inverse transform is implemented very simply by essentially reversing (updating, prediction, and merging in place of splitting) the order of operations in the forward transform. Importantly, the lifting scheme adjusts well to boundary conditions and irregular sampling. SGWs are a generalization of biorthogonal wavelets (traditional biorthogonal wavelets have difficulty dealing with boundaries) and form a Riesz basis for some function spaces (Sweldens, 1998; Sweldens and Schröder, 1996; Vanraes et al., 2002). SGWs have recently been used to solve a system of nonlinear partial differential equations with complicated boundary conditions by using a process of grid adaptation and thresholding to control the error in approximation (Vasilyev and Bowman, 2000).

The area where filter banks and wavelets have had the most visible impact is compression. At the other end of the application spectrum, since 2000, FGWs have been used to attain super-resolution from image and video sequences. The importance of the choice of the mother wavelet and mother scaling function in different applications has been pointed out recently. For example, the optimum wavelet providing the maximum compression ratio and least encoding delay (compression-speed tradeoff) for audio signals from stringed instruments like the sitar was found to be the biorthogonal spline wavelet whereas for audio signals from castanets, the Daubechies wavelet was optimum (Sathidevi and Venkataramani, 2002).

**B. Introduction.** Techniques for enhancing the resolution by processing the acquired images shifted by fraction of a pixel (subpixel) with respect to each other are well documented. To cite a few,

Correspondence to: N. K. Bose; e-mail: nkb@stspbk.ee.psu.edu  
Research supported by Army Research Office Grant DAAD 19-03-1-0261.

Poletto and Nicolosi (1999) developed a high-resolution reconstruction algorithm insensitive to high uncertainties in the relative subpixel displacements of the low-resolution frames and to a low signal-to-noise ratio. Shift information of the sampling lattices in high-resolution reconstruction (image sequence super-resolution) is extracted from a given image sequence, static or dynamic, through subpixel accuracy. In dynamic image reconstruction, motion compensation is needed before subpixel shift information can be extracted from the sequence. A survey of several subpixel accuracy image registration algorithms for, especially, machine vision algorithms is available in Kim and Su (1993). In Su and Kim (1994), for each block image in a reference frame, motion estimation and subpixel registration are performed against adjacent frames, prior to high-resolution reconstruction from dynamic image sequences.

Algorithms have been proposed that use subpixel shifts between a sequence of captured images [low-resolution (LR) frames] to estimate a single high-resolution (HR) image, called a super-resolved image. This process has been referred to as microscanning (Gillett, et al., 1995). Such subpixel shifts may occur due to random variation between the objects in a scene and camera motion. The sampling of the scene is thus nonuniform, and the shifts are combined so that an image that is effectively sampled at a higher rate than the individual frames is constructed. Improved resolution from subpixel shifted pictures was also obtained (Ur and Gross, 1992) by using a multichannel generalized sampling theorem. The need for subpixel displacements was apparent in the recursive algorithms developed for HR reconstruction from LR frames in the presence not only of observation error but also error in estimation of the unknown shift parameters (Bose et al., 1993). For subpixel motion estimation the work of Schultz et al. (1998) is also relevant. Bose and Boo (1998) presented a mathematical model for constructing an HR image from LR images acquired through a multisensor array. Subpixel shifts were needed in this model and, therefore, in subsequent research that used the model, (e.g., Chan et al., 2003; Ng et al., 2002).

In the early work on wavelet superresolution, the important problem of mother wavelet selection was neglected (Nguyen and Milanfar, 2000). The finitely supported families evaluated for the task of image sequence super-resolution [discussed in Lertrattanapich (2003)] for optimum selection of mother wavelet included Haar, Daubechies, Symlets, Coiflets, and B-splines. The common desirable properties of mother scaling function and wavelet—including finite small support (to reduce computational chore), explicit and simple expression, symmetry (or linear phase), orthogonality or biorthogonality, high regularity (smoothness), low approximation error, and high time—frequency localization—are best satisfied by B-splines among the classes considered.

## II. OBJECTIVE

The basic idea of second-generation wavelets (SGWs) is to sacrifice translation and dilation in order to construct wavelets adapted to general settings, but to simultaneously preserve many powerful properties of first-generation wavelets (FGWs) such as time—frequency localization, orthogonality or biorthogonality, and fast transforms. It has been noted quite recently that SGWs are inherently more suited for image super-resolution. In Bose et al. (2004), the HR reconstruction with noise reduction was restricted to semi-regular grids (sampling lattices) [tensor product of 1D irregular grids (sampling lattices)]; consequently, the LR frames were displaced only by translations from a reference frame, as approximated in far-field imaging—e.g., satellite imaging or aerial photography.

In the research reported here, attention is focused on achieving super-resolution from registered noisy LR frames without any assumptions on grid (sampling lattice) structure: that is, the procedure will be able to handle arbitrary irregular grids (sampling lattices), although the subpixel displacement assumption, which is justified in super-resolution algorithms, will be maintained. A consequence of the use of arbitrary grids will be the ability to incorporate the more general projective camera motion model into the framework. *The ability to handle arbitrary sampling lattices results from the use of 2D prediction and update operators as opposed to the tensor product of 1D operators used by Bose et al. (2004).* Furthermore, in the 2D case, the definition of odd and even samples in 1D cannot be directly extended. This subsequently results in the inability to define levels of a multiresolution decomposition in the dyadic sense. Thus, in the SGW setting, only one coefficient per scale is chosen for prediction (Vanraes et al., 2002). The use of genuine 2D methods gives better results, as seen from simulation results presented below.

## III. PREPROCESSING PROCESS FOR SUPER-RESOLUTION ALGORITHM

**A. Singularity Prevention.** In the super-resolution problem, after registering all samples in LR images into a HR grid (sampling lattice), it is possible that two samples or more are either transformed to the same location or assumed to be the same because of machine imprecision. In some super-resolution algorithms, certain irregular sampling structures in a HR grid (sampling lattice) that can lead to a singular problem were identified by Kim and Bose (1990). Therefore, here also, the LR frames that give rise to such singular sampling structures are detected and eliminated before the super-resolution algorithm is implemented.

**B. Bad Frame Elimination.** Another possible problem arises because some LR frames in the sequence may be too badly corrupted by additive noise or severely blurred (or both) to be useful in processing when compared with other frames in the sequence. Such frames are called “bad frames.” These bad frames should be discarded from the sequence because they usually deteriorate the resulting HR image. A rationale for identifying the bad frames has been advanced recently by Lertrattanapich (2003). Because most parts of LR frames usually contain the same region of interest (ROI), the variances of these LR frames in the sequence should be more or less the same unless they are bad frames. Note that the sample variance  $\sigma_k^2$  of the  $k$ th  $M \times N$  LR frame  $f_k[i, j]$  used here is defined as

$$\sigma_k^2 = \frac{1}{MN-1} \sum_{i=0}^{M-1} \sum_{j=0}^{N-1} (f_k[i, j] - \mu_k)^2, \quad (1)$$

where

$$\mu_k = \frac{1}{MN} \sum_{i=0}^{M-1} \sum_{j=0}^{N-1} f_k[i, j] \quad (2)$$

is the sample mean of the  $k$ th LR frame  $f_k[i, j]$ .

Intuitively, the bad frames that are badly corrupted by additive noise have higher variance than acceptable LR frames. In contrast, the variances of the bad frames that are severely blurred by some PSFs are lower than those of acceptable LR frames. This expectation

has been substantiated by numerous simulations (Lertrattanapanich, 2003) and has been useful in the identification and subsequent removal of bad frames.

#### IV. SUPER-RESOLUTION ALGORITHM USING SGWs

In this section, an algorithmic description of the process for obtaining a super-resolved image from a set of LR images based on SGWs and the lifting technique (Sweldens, 1998) is presented. Lifting is a general technique that can be used for the construction of FGWs and SGWs. *FGWs can also be constructed using filter banks, but SGWs can only be constructed using the lifting technique.* The algorithm presented represents a new and seemingly natural approach to super-resolution. In addition, noise filtering is simultaneously implemented.

**Assumptions:** The main assumption made is that the LR frames have subpixel displacements with respect to a chosen reference LR frame, which is a valid assumption in the super-resolution framework (see e.g., Schultz et al., 1998; Ur and Gross, 1992).

A secondary assumption is that the LR frames are either already registered or their registration matrices (projective camera motion model parameter matrices) are known by the use of standard procedures (Lertrattanapanich, 2003; Lertrattanapanich and Bose, 2002; Mann and Picard, 1997).

Let  $LR_i[m, n]$ ,  $i = 1, 2, \dots, r, \dots, K$  represent the LR frames, where  $LR_r$  denotes the reference LR frame. The coordinate system considered is with respect to  $LR_r$ . Let  $f[m, n]$  denote the registered image obtained using a preselected subset  $K_1 \subseteq \{1, 2, \dots, K\}$  of the available noisy frames. Let  $s[m, n]$  denote the super-resolved image that exists on a regular HR grid, the coordinates of which are defined by the rows of a matrix  $H$ . The order,  $N$ , of subdivision is determined by the bivariate polynomial of partial degree  $(N - 1)$  in each variable used for prediction and can be shown (Sweldens, 1998) to correspond to the number of vanishing moments of the dual wavelet (counterpart of scaling function in FGW),  $\varphi$ . The number of vanishing moments of the primal wavelet,  $\psi$ ,  $\tilde{N}$ , is chosen in the update step. *A closed form expression cannot be given for the dual and primal wavelets (unlike in some FGWs like B-spline based)* because, in the general second-generation setting, wavelets are custom built to fit the given samples, and hence are arbitrary. In the simulation results presented here,  $N = 2$ ,  $\tilde{N} = 1$ , because a 1-ring neighborhood is used for prediction (note that for higher values of  $N$  and  $\tilde{N}$ , a larger neighborhood will be required to ensure a full rank overdetermined system, used here, in the prediction operation described subsequently). Reasons for the choice of a 1-ring neighborhood in place of a 1-ring neighborhood with flaps are presented in the algorithm given below. Other higher-order neighborhoods, such as the 2-ring neighborhood, are supersets of the 1-ring neighborhood with flaps, and hence cannot be used for the same reasons as given for the 1-ring neighborhood with flaps.

The least squares prediction at a generic point  $[m_0, n_0]$  can be viewed as the value at  $[m_0, n_0]$  of the surface that fits, in a least squares sense, the points in  $N_{m_0 n_0}$ , the 1-ring 2D neighborhood of  $[m_0, n_0]$ . Let  $\mathbf{m} = [m_1, \dots, m_N]^T$  and  $\mathbf{n} = [n_1, \dots, n_N]^T$ , represent the vectors associated with the points belonging to  $N_{m_0 n_0}$ , where  $N$  is the number of points in  $N_{m_0 n_0}$ . Let  $\mathbf{s}$  represent the corresponding vector of scaling function coefficients. The model for the surface (a plane in this case since  $N = 2$ ) is given by

$$s = \alpha_0 + \alpha_1 m + \alpha_2 n + e,$$

where  $e$  is the error in the fit with mean  $E\{e\} = 0$ . The minimum norm least squares estimate of  $\boldsymbol{\alpha} = [\alpha_0 \ \alpha_1 \ \alpha_2]$  is given by

$$\hat{\boldsymbol{\alpha}} = (\mathbf{P}^T \mathbf{P})^{-1} \mathbf{P}^T \mathbf{s},$$

where the matrix  $\mathbf{P} = [\mathbf{1} \ \mathbf{m} \ \mathbf{n}]$  and  $\mathbf{1}$  is a vector of 1's. The prediction at a generic point  $[m_0, n_0]$  is then computed as the dot product

$$\hat{s}_0 = [1 \ m_0 \ n_0] \cdot \hat{\boldsymbol{\alpha}}.$$

The detail coefficient that replaces the original value  $s_0$  at  $[m_0, n_0]$  is then computed as

$$d_0 = s_0 - \hat{s}_0. \quad (3)$$

The update operator can be described by the vector  $\mathbf{u} = [u_1, \dots, u_N]$  where each of the  $u_i$ 's is computed so that its  $\ell_2$ -norm is minimized using the equation (Delouille et al., 2003; Jansen et al., 2001),

$$u_i = \frac{A_i A_0^*}{\sum_{k=1}^N (A_k)^2}, \quad (4)$$

where  $A_0^*$  is the support area of  $\phi$  around the point  $[m_0, n_0]$  and  $A_i$  denotes the corresponding area around point  $i \in N_{m_0 n_0}$  after the grid has been coarsened by the removal of the predicted point  $[m_0, n_0]$ . Subsequently, each scaling function coefficient,  $s_k$ , is updated according to a set of equations associated with all the detail coefficients predicted using  $s_k$ . A typical member of this set associated with the generic point  $[m_0, n_0]$  is

$$d_0 = s_0 - \sum_{k=1}^N s_k u_k. \quad (5)$$

#### A. Algorithm.

- If  $f[m, n]$  is not given, obtain  $f[m, n]$  using the known registration matrices of  $LR_i[m, n]$ ,  $i \in K_1$  on the coordinate system  $\mathbb{R} \times \mathbb{R}$  defined with respect to  $LR_r$ . The grid (sampling lattice) (on which  $f[m, n]$  exists) so obtained is an irregularly sampled grid (sampling lattice).
- Define the required high-resolution grid (sampling lattice) in the coordinate system defined above, that is, determine the matrix  $H$ . Split  $H$  into two sets of points, one set,  $H_u$ , comprised of points whose values are to be updated and retained in the subsequent steps of the algorithm, and another set,  $H_p$ , which is to be predicted and eliminated from the coarse representation of  $f[m, n]$  developed below.
- Compute the Delaunay triangulation (Okabe et al., 1992) of the points defining  $f[m, n]$ .
- For each point in the set  $H_p$ , say  $[m_0, n_0]$ :
  - Determine the points in the 1-ring neighborhood (Figure 1),  $N_{m_0 n_0}$ , to the extent possible. The use of a 1-ring neighborhood with flaps for prediction was documented by Delouille et al. (2003). But this was not employed because the assumption of subpixel displacement of the LR frames tends to result in a triangulation with flap points that are usually nearly collinear with the points in the 1-ring neighborhood. This may lead to ill conditioning of the prediction matrix which, consequently, causes instability in the implementation of the prediction operator.

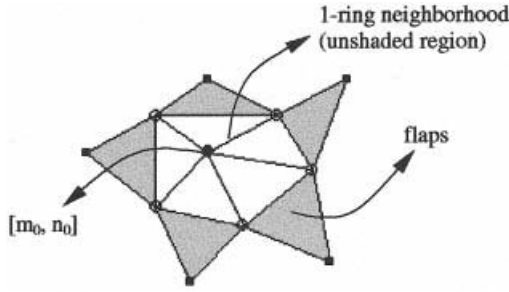


**Figure 1.** 1-ring neighborhood with flaps.

- Compute the prediction at  $[m_0, n_0]$  by means of a least squares predictor, described above [boundary points are handled differently as in, for example], Delouille et al. (2003), using points in  $N_{m_0, n_0}$ . Subsequently, replace the scaling function coefficient at  $[m_0, n_0]$  by the detail coefficient in Eq. (3).
- Determine  $A_0^*$ , the support area of the scaling function around  $[m_0, n_0]$ . This can be determined as the sum of one-third the area of the triangles with common vertex  $[m_0, n_0]$ .
- Delete  $[m_0, n_0]$  from the triangulation resulting in a coarser grid (sampling lattice)
- Compute the corresponding areas,  $A_k$ ,  $k = 1, \dots, N$ , of the cells around points belonging to  $N_{m_0, n_0}$  in the coarsened grid.
- Compute the minimum norm update operator as in Eq. (4) and update the scaling function coefficients at points belonging to  $N_{m_0, n_0}$ , as in Eq. (5).
- A second-generation 2D wavelet surface has now been defined on the irregularly sampled registered grid (sampling lattice).
- The detail coefficient values at the points on the HR grid (sampling lattice) can now be computed either by ignoring the irregularity of the grid and assigning the value of the closest irregular point (no significant loss of accuracy due to subpixel displacement assumption) or by resampling the wavelet (not scaling function).

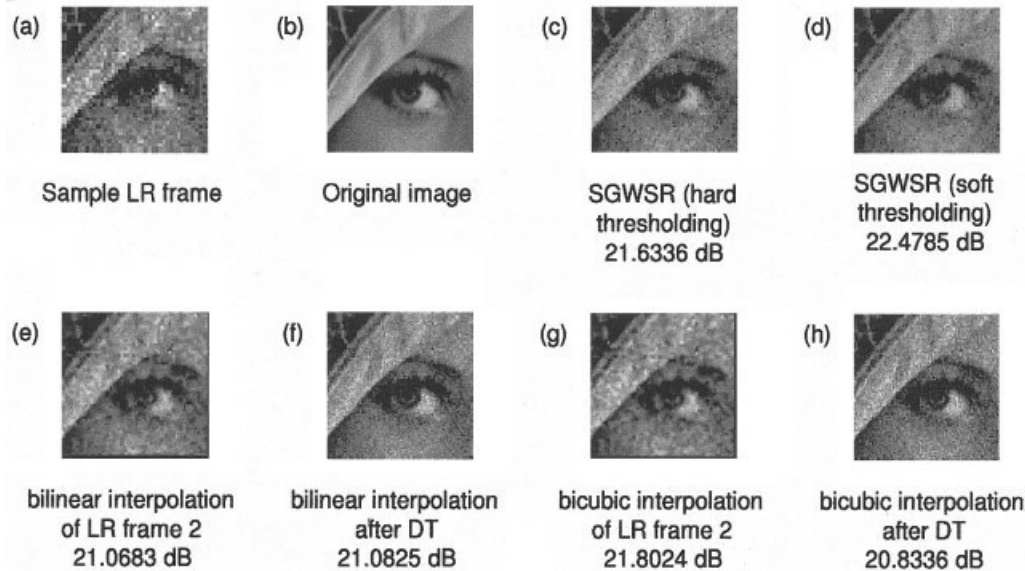
- To achieve noise reduction, the wavelet/detail coefficients computed are subjected to thresholding (Jansen, 2001; Vanraes et al., 2002).
- The inverse lifting procedure is now applied on the HR grid (sampling lattice) to obtain the super-resolved image  $s[m, n]$ .

## V. SIMULATION RESULTS

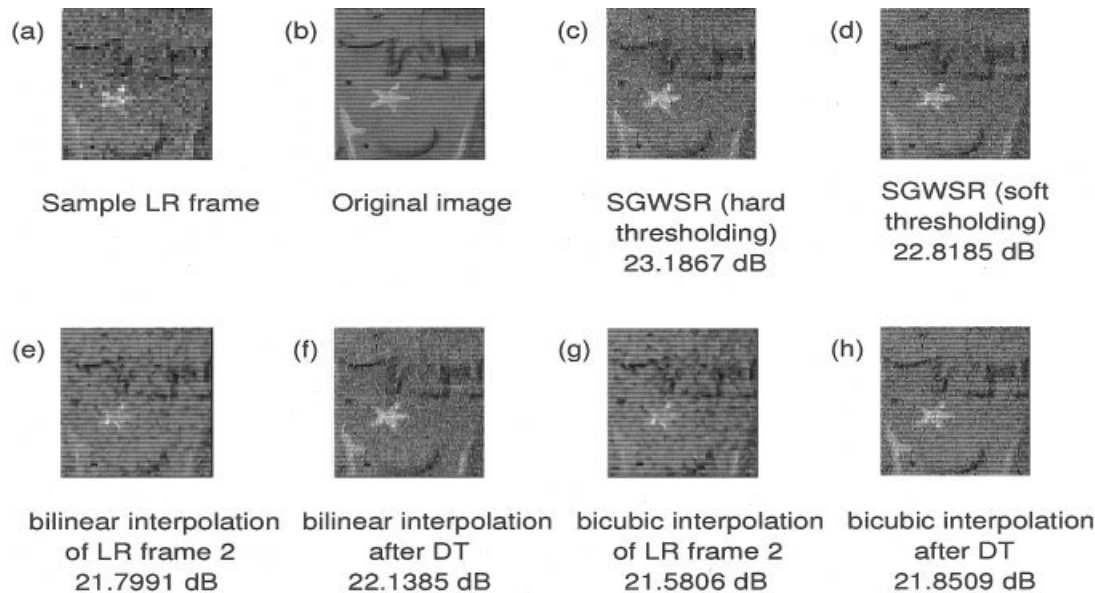
Results obtained by the use of the SGW-based algorithm described in the preceding section are presented and discussed below. The LR frames used in the simulation were of size  $40 \times 40$  pixels and were generated using an  $80 \times 80$  image by downsampling and low-pass filtering. Further, the LR frames are all displaced with respect to each other, but unlike the results presented by Bose et al. (2004) (in which the displacements were restricted to only translations), the displacements follow the more general projective model. The LR frames were also corrupted by AWGN of variance 0.1. As mentioned earlier, in the simulations presented in this section, the number of vanishing moments of the dual and primal wavelets,  $N$  and  $\tilde{N}$  respectively, are 2 and 1.

Figure 2 shows the results from one simulation. In this case, six LR frames were used and a resolution improvement factor of 2 in each dimension was chosen. It is noted that the use of higher number of LR frames leads not only to higher resolution factors, but also to improved noise reduction. A sample LR frame is shown in Figure 2(a) and the original image is shown in Figure 2(b). The SGW-based high-resolution reconstructions using hard and soft thresholding are shown in Figures 2(c) and 2(d), respectively. For comparison, four other high-resolution reconstructions based on surface approximation (bilinear and bicubic) of a single LR frame gives the visually worst results, although their PSNR value is comparable to the others. The Delaunay triangulation-based methods give much better results but cannot simultaneously achieve noise filtering.

Results for another image are shown in Figure 3. As in the previous result, six LR frames are used and the resolution improvement factor is set to 2 in each dimension. Panel (a) shows a sample LR frame. The original image is shown in Figure 3(b). The SGW-



**Figure 2.** Simulation result 1 with PSNR in dB.



**Figure 3.** Simulation result 2 with PSNR in dB.

based HR reconstructions with noise reduction achieved using hard and soft thresholding of wavelet coefficients are shown in Figures 3(c) and 3(d), respectively. Similar to the previous result presented, surface interpolation based reconstructions are given in Figures 3(e)–(h).

In both the results presented, a point to be noted is the retention of a reasonably high degree of sharpness in the noise-filtered SGW-based reconstructions. This is in contrast to other noise filtering techniques such as averaging and low-pass filtering, which typically result in smoothing of edges.

To enable comparison and differentiation of the techniques presented in this article and in Bose et al. (2004), results generated by both the methods applied to the same data set are presented in Figure

4. In this simulation, the displacements of the LR frames were restricted to translations [required to run the algorithm given by Bose et al. (2004)] and four LR frames were used. The LR frames were corrupted by AWGN of a very low variance of 0.05. In both methods,  $N = 2$ ,  $\tilde{N} = 1$ . Panels (a) and (b) give a sample LR frame and the original image respectively. Figures 4(c) and 4(d) show the reconstructions obtained by treating the registered image  $f[m, n]$  as the tensor product of two 1D vectors. On treatment of  $f[m, n]$  in the 2D sense, the HR images obtained are given in Figures 4(g) and 4(h). It is important to observe that although the two sets of results have very close PSNR values, the results obtained using the algorithm presented here are much sharper. For comparison, the results obtained using bilinear and bicubic surface interpolation after

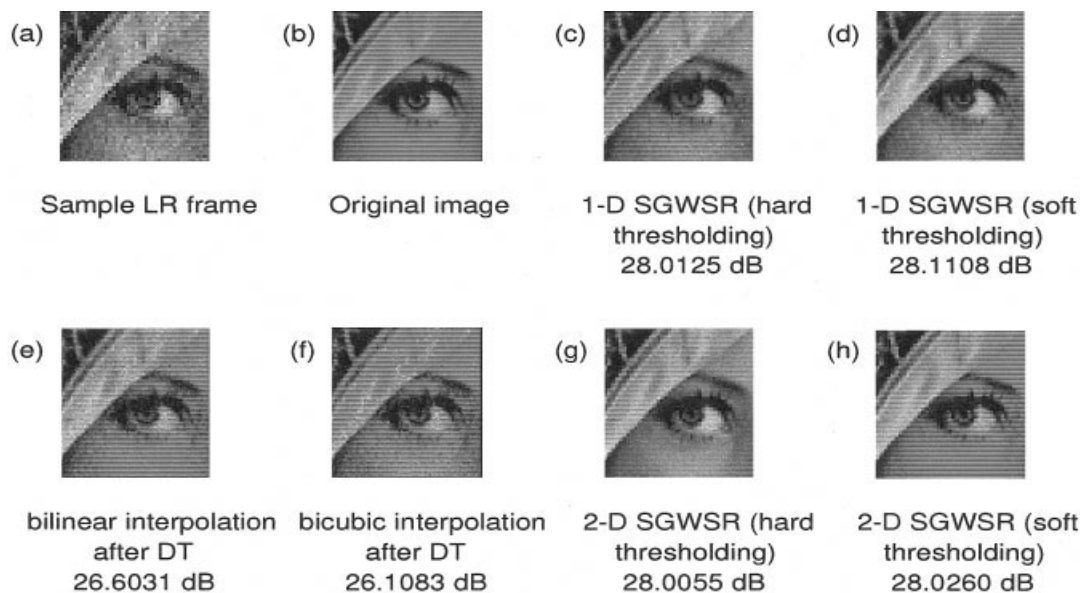


**Figure 4.** Comparison of 1D (Bose et al., 2004) and 2D SGWSR algorithms with PSNR in dB.



Delaunay triangulation are given in Figures 4(e) and 4(f), respectively. Clearly, both the SGWSR methods outperform the surface interpolation methods.

## VI. CONCLUSIONS

A framework for achieving image sequence super-resolution simultaneously with noise filtering has been developed using SGWs coupled with hard or soft thresholding. The procedure works well when the noisy images acquired by sensors are not severely blurred. A topic of future research is the embedding of a technical device into the procedure to adequately overcome the degrading effects of blur, when present to a significant extent. The problem is reminiscent to that faced in earlier works on super-resolution. For example, in the early DFT-based procedure (Kim and Bose, 1990), interpolation and noise filtering were simultaneously implemented and it was later shown that blur distortions in the input images can be compensated with regularization during reconstruction (Kim and Su, 1993). In recent super-resolution work, multiframe blur identification followed by deblurring has been done in a separate module from the super-resolution and noise filtering modules (Lertrattanapanich and Bose, 2002).

The procedure depends on subpixel accuracy image registration. For dynamic image sequences, motion compensation is necessary prior to that and, although the algorithm presented here applies to arbitrary nonuniform shift grids (sampling lattices), its robustness to errors in estimation of motion parameters is another topic of future research.

The main advantage of the procedure is that the speed of implementation provided by the lifting technique (surface approximation methods (Lertrattanapanich and Bose, 2002) may be faster but do not incorporate noise filtering), the adaptation to arbitrary nonuniform sampling lattice (especially relevant in dynamic image sequences), the absence of a priori assumptions on boundary conditions (zero, periodic, Neumann have given progressively better results over the years but make assumptions that are unnecessary here), and the independence from proper choice of mother wavelets and scaling functions which makes SGW-based super-resolution methods potentially more suitable in multimedia applications.

## ACKNOWLEDGEMENT

The constructive comments of the reviewer that improved the clarity of presentation is gratefully acknowledged. The support provided by Army Research Office Grant DAAD 19-03-1-0261 is gratefully acknowledged.

## REFERENCES

N. K. Bose, K. J. Boo. 1998. High-resolution image reconstruction with multisensors. *Int J Imaging Syst Technol* 9:294–304.

N. K. Bose, H. C. Kim, H. M. Valenzuela. 1993. Recursive total least squares algorithm for image reconstruction from noisy, undersampled frames. *Multidimensional Syst Signal Processing* 4(3):253–268.

N. K. Bose, S. Lertrattanapanich. 2004. Polynomial matrix factorization, multidimensional filter banks, and wavelets. In: J. J. Benedetto, A. I. Zayed, Eds. *Sampling, wavelets, and tomography*, Boston: Birkhaeuser, 2004, pp. 137–156.

N. K. Bose, S. Lertrattanapanich, M. B. Chappalli. 2004. Super-resolution with second generation wavelets. *Signal Processing: Image Commun* 19(5): 387–391.

R. Chan, T. Chan, L. Shen, Z. Shen. 2003. Wavelet algorithms for high resolution image reconstruction. *SIAM J Scient Comput* 24(5):1408–1432.

V. Delouille, M. Jansen, R. von Sachs. 2003. Second generation wavelet methods for denoising of irregularly spaced data in two dimensions. Technical Report 0303, Institut de Statistique, Université Catholique de Louvain, <http://www.stat.ucl.ac.be/ISpub/tr/2003/TR0303.pdf>, 2003.

J. C. Gillett, T. M. Stadtmiller, R. C. Hardie. 1995. Aliasing reduction in staring infrared images utilizing subpixel techniques. *Opt Eng* 34(11):3130–3137.

M. Jansen. 2001. *Noise Reduction by Wavelet Thresholding*. Vol. 161, Lecture Notes in Statistics. Springer Verlag: New York, 2001.

M. Jansen, G. Nason, B. Silverman. 2001. Scattered data smoothing by empirical Bayesian shrinkage of second generation wavelet coefficients. In: Unser M, Aldroubi A, Eds. *Wavelet applications in signal and image processing*. IX Proceedings of SPIE, Vol. 4478, 2001, pp. 87–97.

S. P. Kim, N. K. Bose. 1990. Reconstruction of 2-D bandlimited discrete signals from nonuniform samples. *IEE Proc* 137(3):197–204.

S. P. Kim, W. Y. Su. 1993. Recursive high-resolution reconstruction of blurred multiframe images. *IEEE Trans Image Processing* 2(4):534–539.

S. Lertrattanapanich. 2003. Superresolution from degraded image sequence using spatial tessellations and wavelets. PhD thesis, Department of Electrical Engineering, The Pennsylvania State University, University Park, PA, 16802.

S. Lertrattanapanich, N. K. Bose. 2002. High resolution image formation from low resolution frames using Delaunay triangulation. *IEEE Trans Image Processing* 11(12):1427–1441.

S. Mann, R. W. Picard. 1997. Video orbits of the projective group: A simple approach to featureless estimation of parameters. *IEEE Trans Image Processing* 6(9):1281–1295.

M. Ng, N. K. Bose, J. Koo. 2002. Constrained total least squares computations for high resolution image reconstruction with multisensors. *Int J Imaging Syst Technol* 12(5):35–42.

N. Nguyen, P. Milanfar. 2000. A wavelet-based interpolation-restoration method for super-resolution (wavelet superresolution). *Circuits, Syst Signal Process* 19(4):321–338.

A. Okabe, B. Boots, K. Sugihara. 1992. *Spatial Tessellations: Concepts and Applications of Voronoi Diagrams*. John Wiley: New York, 1992.

L. Poletto, P. Nicolosi. 1999. Enhancing the spatial resolution of a two-dimensional discrete array detector. *Opt Eng* 38(10):1748–1757.

P. S. Sathidevi, Y. Venkataramani. 2002. Perceptual audio coding using sinusoidal/optimum wavelet representation. *Circuits, Syst Signal Processing* 21(5):511–524.

R. Schultz, L. Meng, R. L. Stevenson. 1998. Subpixel motion estimation for super-resolution image sequence enhancement. *J Visual Commun Image Represent* 9(1):38–50.

W. Y. Su, S. P. Kim. 1994. High-resolution restoration of dynamic image sequences. *Int J Imaging Syst Technol* 5:330–339.

W. Sweldens. 1998. The lifting scheme: A construction of second generation wavelets. *SIAM J Mathe Anal* 29(2):511–546.

W. Sweldens, P. Schröder. 1996. Building your own wavelets at home. In: *Wavelets in computer graphics*, ACM SIGGRAPH Course Notes, 1996, pp. 15–87.

H. Ur, D. Gross. 1992. Improving resolution from subpixel shifted pictures. *CVGIP: Graphical Models for Image Process* 54(2):181–186.

E. Vanraes, M. Jansen, A. Bultheel. 2002. Stabilised wavelet transforms for non-equispaced data smoothing. *Signal Process* 82(12):1979–1990.

O. V. Vasilyev, C. Bowman. 2000. A second-generation wavelet collocation method for the solution of partial differential equations. *J Comput Phys* 165:660–693.

J. Windmolders, E. Vanraes, P. Dierckx, A. Bultheel. 2003. Uniform Powell–Sabine spline wavelets. *J Computat Appl Math* 154(1):125–142.

# Simultaneous Noise Filtering and Super-Resolution with Second-Generation Wavelets

Mahesh B. Chappalli, *Student Member, IEEE* and N. K. Bose, *Fellow, IEEE*

**Abstract**—Wavelet coefficient thresholding is effective in reducing spatial domain noise in wavelet-based super-resolution algorithms. Here, the effect of the threshold level on reconstructed image quality in second-generation wavelet super-resolution is investigated. The choice of optimal threshold involves a trade-off between noise filtering and blurring introduced by thresholding. A measure based on the singular values of the image matrix is employed as a reliable gauge of generated high-resolution image quality.

**Index Terms**—Noise filtering, second-generation wavelets, super-resolution, thresholding.

## I. INTRODUCTION

In this letter, the term “super-resolution” refers to algorithms that produce a high-resolution (HR) image by combining information from a captured sequence of low-resolution (LR) frames. Due to various factors like imperfections in the acquisition device, limited resolution of the physical sensing elements, motion, and medium turbulence, the LR frames are blurred and noisy. Hence, super-resolution algorithms commonly include noise filtering and deblurring modules. The focus of this letter is to improve the performance of the second-generation wavelet super-resolution (SGWSR) algorithms given initially in [1] and in a more general two-dimensional (2-D) setting in [2], though some of the results presented apply to wavelet denoising in general. The aim is to remove as much of the corrupting noise as possible without adversely affecting the reconstructed image quality due to blur introduced in the process. Though there are many techniques for denoising images (for example [3], [4], [5] and [6]), some of which consider optimal thresholding, the denoising technique based on wavelet coefficient thresholding [7] is selected here because this allows simultaneous noise filtering and superresolution thereby reducing computation cost in the overall framework. Most of the earlier methods dealing with optimal thresholding of wavelet coefficients adopt a quality metric based on mean-squared error (MSE), which does not necessarily yield the best visual quality. The optimal threshold for denoising based on wavelet coefficient thresholding is obtained in this paper in terms of the visual quality defined by

a metric that matches the human visual system (HVS) better than other metrics [8]. The SGWSR methods simultaneously incorporate noise filtering by hard/soft thresholding of wavelet coefficients defined, respectively, by the following expressions [7]:

$$d_h = \begin{cases} d, & d > \zeta \\ 0, & d \leq \zeta \end{cases}, \quad d_s = \begin{cases} d - \zeta, & d > \zeta \\ 0, & d \leq \zeta \end{cases}, \quad (1)$$

where  $d$  represents the SGW coefficients before thresholding and  $\zeta$  is the threshold. Soft thresholding, known to yield better results [1], [2], is used in this paper. The algorithms in [1], [2] did not investigate the optimal choice of threshold,  $\zeta$ . It is important to note that thresholding in the SGW setting is much more challenging than in the first-generation wavelet (FGW) case since small coefficients may carry important information which is essential for a stable inverse transform [9]. The trade-off between blur introduced by thresholding and input noise mandates the need to find an optimal threshold as explained in Section II. Section III substantiates why peak signal-to-noise ratio (PSNR) and the universal image quality index  $Q$  [10] are unsuitable as measures of visual quality of an image. An image quality measure based on the singular values of the image matrix is then used to assess the effects of thresholding on reconstructed image quality in Section IV. Finally, conclusions are presented in Section V.

## II. THRESHOLDING SGW COEFFICIENTS

A set of sub-pixel shifted frames,  $\{f_k\}, k = 1, 2, \dots, K$  (of size  $n_1 \times n_2$ ) of the same object/scene, generated with small variation in camera motion and position, and captured under the same imaging conditions should have approximately the same variance,  $\sigma_k^2$ , and mean,  $\mu_k$ , given by

$$\sigma_k^2 = \frac{1}{n_1 n_2 - 1} \sum_{i=0}^{n_1-1} \sum_{j=0}^{n_2-1} (f_k[i, j] - \mu_k)^2, \quad (2)$$

$$\mu_k = \frac{1}{n_1 n_2} \sum_{i=0}^{n_1-1} \sum_{j=0}^{n_2-1} f_k[i, j]. \quad (3)$$

When zero-mean additive white noise is present, the variance of the corrupted frame,  $\tilde{f}_k$ , will be given by

$$\tilde{\sigma}_k^2 = \sigma_k^2 + \eta^2, \quad (4)$$

where  $\eta^2$  is the variance of the noise. A severe additive noise is one whose variance is high. Therefore, a frame which is corrupted by a severe noise will have a variance much higher than that of a frame with a high SNR. Blurring an image with a point spread function (PSF)  $h[p, q]$ , of support  $m_1 \times m_2$ , is

Manuscript received May 7, 2005; revised June 13, 2005. This work was supported by Army Research Office Grant DAAD 19-03-1-0261. The associate editor coordinating the review of this manuscript and approving it for publication was Prof. Lina J. Karam.

The authors are with the Spatial and Temporal Signal Processing Center, Department of Electrical Engineering, The Pennsylvania State University, University Park, PA 16802, USA (e-mail: m.chappalli@samsung.com; nkb@stspbk.ee.psu.edu).

Digital Object Identifier 10.1109/LSP.2005.856875

viewed as low-pass filtering of the image. The variance of the blurred frame,  $\tilde{f}_k$ , can be proved to be

$$\tilde{\sigma}_k^2 = \frac{1}{n_1 n_2 - 1} \sum_{i=0}^{n_1-1} \sum_{j=0}^{n_2-1} \sum_{p=0}^{m_1-1} \sum_{q=0}^{m_2-1} \sum_{r=0}^{m_1-1} \sum_{s=0}^{m_2-1} h[p, q] h[r, s] C_{f_k}[(p, r); (q, s)], \quad (5)$$

where  $C_{f_k}$  is the autocovariance of the original image,  $f_k$ . If the PSF is assumed to sum to unity over its support, then  $\tilde{\sigma}_k^2 \leq \sigma_k^2$  since  $|C_{f_k}[(p, r); (q, s)]| \leq C_{f_k}[(p, p); (q, q)] = \sigma_k^2$ . Consequently, blur tends to reduce the variance unlike noise, which as seen from (4), increases the variance.

The opposing effects of blur and noise on the variance also hold when the SGW coefficients are thresholded. Similar to the FGW setting, the noise corrupting an image is carried over into the SGW coefficients on application of the forward transform. This is readily seen from the expression for the computation of the SGW coefficients (based on lifting [11]) given by

$$d_{-1}[i, j] = (s_0[i, j] + \bar{n}[i, j]) - P\{\mathcal{N}_{[i, j]}\}, \quad (6)$$

where  $s_0[i, j]$  is the pixel value at location  $[i, j]$ ,  $\bar{n}[i, j]$

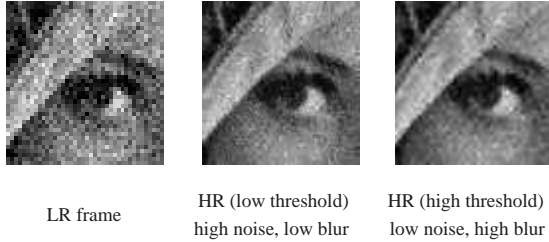


Fig. 1. Effect of threshold on input noise and blur introduced by thresholding

represents random white noise,  $d_{-1}[i, j]$  is the computed SGW coefficient, and  $P$  is the prediction operator that operates on  $\mathcal{N}_{[i, j]}$ , the specified neighborhood of point  $[i, j]$ . A detailed description of the process of prediction for SGWSR is given in [2]. The prediction operator,  $P$ , fails to predict the white noise which propagates to the SGW coefficient  $d_{-1}[i, j]$  in (6). Thus, thresholding of the wavelet coefficients reduces the noise in the reconstruction. However, high wavenumber information in the SGW coefficients may be eliminated by thresholding leading to possibly significant blurring of the reconstructed image. Thus, a need for an optimal choice of the threshold exists. Fig. 1 illustrates the above points.

### III. IMAGE QUALITY MEASURES

PSNR and MSE are the most commonly used measures for comparative image quality. They are defined for normalized  $n_1 \times n_2$  images as

$$\text{MSE} = \frac{\sum_i \sum_j (\tilde{f}[i, j] - f[i, j])^2}{n_1 n_2}, \quad (7)$$

$$\text{PSNR} = 20 \log_{10} \left( \frac{1}{\sqrt{\text{MSE}}} \right), \quad (8)$$

where  $f$  and  $\tilde{f}$  represent the original image<sup>1</sup> and the observation, respectively. Higher PSNR and lower MSE are expected

<sup>1</sup>In real-world problems, the original image is usually inaccessible, which motivates Section IV

to be indicators of better visual quality. However, it is known that PSNR does not match the HVS [12]; that is, higher PSNR does not always imply better visual quality. Studies have shown that the HVS is more sensitive to blurring than to noise. Another image quality measure  $Q$  proposed in [10], though more sensitive to blur than PSNR, was shown by our simulations to be not ideal for determining  $\zeta_{\text{opt}}$ , the optimal threshold, consistent with expectations from results in [8].  $Q$  is defined as [10]

$$Q = \frac{4\sigma_{f\tilde{f}}\mu_f\mu_{\tilde{f}}}{(\sigma_f^2 + \sigma_{\tilde{f}}^2)(\mu_f^2 + \mu_{\tilde{f}}^2)}, \quad (9)$$

where  $\mu_f$  and  $\mu_{\tilde{f}}$  are the means,  $\sigma_f^2$  and  $\sigma_{\tilde{f}}^2$  are the variances of the original and the observed images, respectively, and  $\sigma_{f\tilde{f}}$  is the cross-covariance between the original and the observed images. The plots of PSNR and  $Q$  versus the threshold for an SGWSR reconstruction are shown in Fig. 2. The input to the SGWSR algorithm is a set of six registered LR frames,  $f_k$ , generated from the original image,  $f$ , as

$$f_k = DHT_k f + n_k, \quad k = 1, \dots, 6, \quad (10)$$

where  $T_k$  is the projective transformation,  $H$  is the blur matrix associated with a  $5 \times 5$  truncated Gaussian PSF (note that this blur, which affects the input frames, is different from the blur introduced due to thresholding in the reconstructed HR images),  $D$  is the downsampling matrix, and  $n_k$  is additive white Gaussian noise (AWGN) of variance 0.01. Despite the

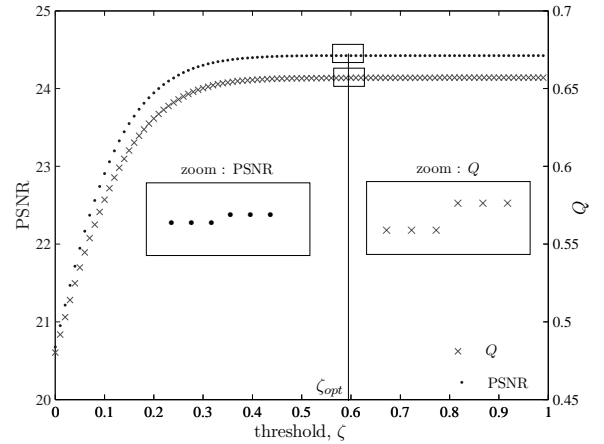


Fig. 2. Effect of threshold on PSNR and  $Q$  in SGWSR

increased blurring and visual quality degradation with higher thresholds (as observed in Fig. 1), both PSNR and  $Q$  measures are inadequate and not sufficiently sensitive to this visual quality change. In Fig. 2, though the curve appears to be perfectly flat before and after the threshold marked as  $\zeta_{\text{opt}}$ , there is a slight increase in PSNR and  $Q$  values at  $\zeta_{\text{opt}}$  (see insets in Fig. 2) after which they remain constant. Flattening of the curve occurs since all wavelet coefficients fall within the threshold as it is increased beyond  $\zeta_{\text{opt}}$ . When considering such flat regions, the minimum possible threshold is selected as  $\zeta_{\text{opt}}$ .

Another measure of image quality based on the singular values of the image matrix was defined as [8]

$$M_{SVD} = \frac{\sum_{j=1}^{k_1 \times k_2} |D_j - D_{med}|}{k_1 \times k_2}, \quad D_j = \sqrt{\sum_{i=1}^p (s_i - \tilde{s}_i)^2}, \quad (11)$$

where  $k_1 = n_1/p$ ,  $k_2 = n_2/p$ ,  $D_{med}$  is the median of the  $D_j$ 's and  $s_i$ ,  $\tilde{s}_i$  are the singular values of the  $j^{\text{th}}$   $p \times p$  block of the original and the observed image matrices, respectively. In [8], it was also shown that the  $M_{SVD}$  measure gives a much better representation of the quality of an image with regard to the HVS for a large variety of distortions. Another point to note is that a lower value of  $M_{SVD}$  indicates better image visual quality. For the same experiment which generated the curves in Fig. 2, the variation of the  $M_{SVD}$  metric for output image quality is as shown in Fig. 3. It is seen that as the threshold

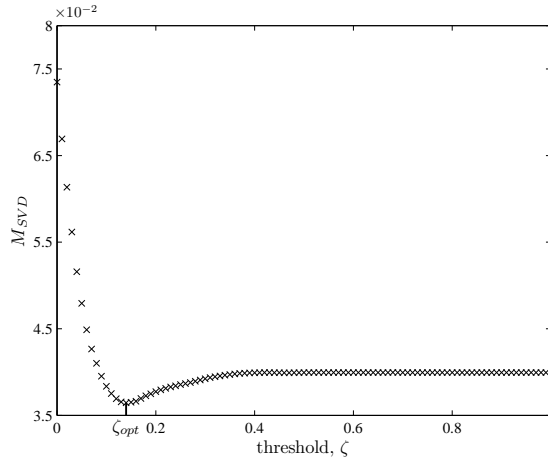


Fig. 3.  $M_{SVD}$  metric based assessment of SGWSR HR image quality

is increased from 0, there is initially (until approximately 0.15) a significant improvement in image quality due to noise reduction, but beyond this, as the effect of blur introduced due to thresholding starts to dominate, the quality of the reconstructed image suffers with increasing threshold. Thus, thresholding involves a trade-off between noise reduction and degree of blur introduced in the reconstructed HR image, and hence, there should exist a threshold value,  $\zeta_{opt}$ , the location of the minimum of the curve in Fig. 3, for which this trade-off is optimal. In other words, the  $M_{SVD}$  metric is sensitive to visual quality degradation due to blur.

#### IV. OPTIMAL THRESHOLD

The **optimal threshold**,  $\zeta_{opt}$ , for the SGWSR algorithms presented in [1], [2], and in general, for any denoising requirement, is the one which minimizes the  $M_{SVD}$  metric defined in (11). Since (11) involves the singular values of a matrix (which cannot, in general, be expressed in terms of the matrix elements), it is not possible to derive a closed-form analytic expression for  $\zeta_{opt}$ . *The optimal threshold is thus obtained by plotting the curve of  $M_{SVD}$  values of the reconstructed HR image for various values of  $\zeta$  and then finding the threshold,  $\zeta_{opt}$ , corresponding to the location of its minimum.*

It is however not practical (in terms of computational effort) to plot such a curve every time the SGW-based (or any other) superresolution algorithm is applied. Furthermore, in most real-world cases, the original image is unavailable for computing the  $M_{SVD}$  or any other metric. The threshold  $\zeta_{opt}$ , which achieves the optimal trade-off between noise reduction and degradation of visual quality due to introduced blur is essentially dependent on the input noise, under the assumption of similar image capture devices and imaging conditions<sup>2</sup>. It follows that, for a specified input noise level,  $\zeta_{opt}$  determined for a small number of training images will be near optimal for other images under similar imaging conditions.

Consider a real-valued  $n_1 \times n_2$  (without loss of generality, assume  $n_1 > n_2$ ) image matrix,  $F = [f[i, j]]$  of rank  $R \leq n_2$ , with singular value decomposition (SVD)

$$U^T F V = \begin{bmatrix} \Sigma & 0 \\ 0 & 0 \end{bmatrix}, \quad \Sigma = \text{diag}(s_1, \dots, s_R), \quad (12)$$

where  $s_1 \geq \dots \geq s_R > 0$  are the singular values of  $F$ . Consider the corruption of the image matrix  $F$  by a zero-mean AWGN matrix  $\tilde{N}$  to get  $\tilde{F} = [\tilde{f}[i, j]] = F + \tilde{N}$ . Let  $\tilde{s}_1 \geq \dots \geq \tilde{s}_R > 0$  be the singular values of  $\tilde{F}$ , which is of rank  $R$ . Then, from [13, pp. 203, Corollary 4.10], it follows that

$$\max_i \{|\tilde{s}_i - s_i|\} \leq \|\tilde{N}\|_2, \quad i = 1, 2, \dots, R, \quad (13)$$

where  $\|\cdot\|_2$  is the matrix 2-norm. A generalization of the above result is due to Mirsky (holds for any unitarily invariant norm) which in the case of Frobenius norm (denoted by the subscript  $Fr$  for the norm) becomes [13, pp. 205, Corollary 4.13]

$$\sum_i (\tilde{s}_i - s_i)^2 \leq \|\tilde{N}\|_{Fr}^2, \quad i = 1, 2, \dots, R. \quad (14)$$

Consequently, from (11),

$$D_j \leq \|\tilde{N}\|_{Fr}. \quad (15)$$

Since (11) involves only  $D_j$ 's, the  $M_{SVD}$  metric is essentially bounded by the norm of the noise matrix,  $\tilde{N} = [\tilde{n}[i, j]]$ . Further, if the singular values of  $F$  are distinct (simple), then under the assumptions of sufficiently small noise [13, pp. 264-266],

$$\tilde{s}_i = s_i + u_i^T \tilde{N} v_i + O(\|\tilde{N}\|_2^2), \quad (16)$$

where  $U = [u_1 \dots u_{n_1}]$  and  $V = [v_1 \dots v_{n_2}]$  in the SVD in (12). Ignoring the higher order terms, the expected value of the sum of squares of the errors in the singular values is

$$E \left\{ \sum_{i=1}^{n_2} (\tilde{s}_i - s_i)^2 \right\} = E \left\{ \sum_{i=1}^{n_2} (u_i^T \tilde{N} v_i)^2 \right\} = R\eta^2, \quad (17)$$

where  $\eta^2$  is the variance of the noise. Thus, the  $M_{SVD}$  metric and consequently, the optimal threshold,  $\zeta_{opt}$ , is dependent, on the average, only on the imaging device and imaging conditions. Therefore, for a given class of devices and relatively

<sup>2</sup>In the superresolution algorithms presented in [1], [2], the input blur is due to the image capture device and is assumed constant. A different input blur thus constitutes a different imaging condition.

fixed imaging conditions, the desired  $\zeta_{opt}$  for the SGWSR algorithm [1], [2] can be approximated by a threshold  $\tilde{\zeta}_{opt}$  computed using a small number of training images.

Simulation results which support the analysis presented above are given in Table I. 70 different HR images were reconstructed from their respective sets of 6 LR frames which were subjected to similar input degradations. The variance of the optimal threshold (which was computed for each of these HR images by plotting a curve and finding the threshold corresponding to its minimum as explained earlier) for these images is noted to be very small. As seen from Table I, for another set of 70 images with different imaging conditions, the optimal threshold, justifiably different, exhibits very low variance, consistent with the analytical result given above.

Training Set	Imaging Conditions	Variance of $\zeta_{opt}$	$\tilde{\zeta}_{opt}$ (median)
70	AWGN of variance 0.001 (5 × 5) input Gaussian blur with variance 1.0	$7.44 \times 10^{-4}$	0.02
70	AWGN of variance 0.01 (5 × 5) input Gaussian blur with variance 0.5	$1.13 \times 10^{-3}$	0.125

TABLE I

VARIANCE OF  $\zeta_{opt}$  FOR DIFFERENT IMAGING CONDITIONS; APPROXIMATE OPTIMAL THRESHOLD,  $\tilde{\zeta}_{opt}$

Finally, a sample LR frame and HR reconstructions, based on the SGWSR algorithm, with the optimal thresholds obtained from the PSNR curve in Fig. 2 and the  $M_{SVD}$  curve in Fig. 3 are shown in Fig. 4. The LR images were subjected to a 5 × 5 Gaussian PSF blur and corrupted by zero-mean AWGN of variance 0.01. The HR images obtained from the SGWSR algorithm based on the optimal threshold derived from the PSNR curve and the  $M_{SVD}$  curve are shown in Fig. 4(c) and (d) respectively. The application of single frame post-deblurring (to offset the effect of input blur as well as blur introduced by thresholding) based on the accelerated Richardson-Lucy algorithm due to Biggs and Andrews [14] (30 iterations) to each HR image in Fig. 4(c) and (d) yields the results in Fig. 4(e) and (f), respectively. The PSNR-based optimal threshold gives better noise filtering but poor deblurring [see Fig. 4(c) and (e)] while the  $M_{SVD}$ -based optimal threshold produces a trade-off between introduced blur and input noise filtering that produces output images with better visual quality [see Fig. 4(d) and (f)]. For the HR image in Fig. 4(d), the optimal threshold  $\zeta_{opt}$ , as per the  $M_{SVD}$  curve plotted for the image was 0.14. From Table I, the near-optimal threshold,  $\tilde{\zeta}_{opt}$  for the imaging conditions for this image (row 2 in the table) is 0.125, which is very close to  $\zeta_{opt}$ . The image quality due to the use of  $\tilde{\zeta}_{opt}$  was found to be almost identical to the ones in Fig. 4(d) and (f) generated using  $\zeta_{opt}$ , supporting the use of near-optimal thresholds.

## V. CONCLUSION

It has been shown that the choice of threshold is important in the SGWSR algorithm. The inadequacy of PSNR and Q

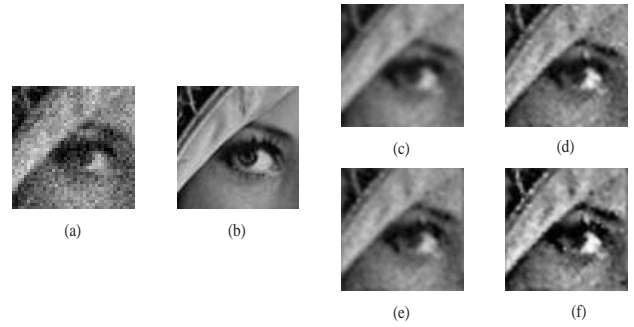


Fig. 4. (a) sample LR image; (b) original image; (c), (d) HR images based on optimal threshold from PSNR and  $M_{SVD}$ , respectively; (e), (f) HR images in (c) and (d), respectively, after post-deblurring of input blur

for quantifying visual image quality prompted the use of the  $M_{SVD}$  metric to determine the threshold for optimal trade-off between the blur introduced by thresholding and input noise reduction in the reconstructed HR image. Supporting analysis and simulation results are given. Subsequently, the use of near-optimal thresholds (which depend on the imaging conditions rather than the images) is proposed for improving the visual quality of HR reconstructions in the SGWSR algorithms.

**Acknowledgement:** The authors thank Dr. Lina Karam and the reviewers for their prompt and constructive evaluation.

## REFERENCES

- [1] N. K. Bose, S. Lertrattanapanich, and M. B. Chappalli, "Superresolution with second generation wavelets," *Signal Processing: Image Comm.*, vol. 19, no. 5, pp. 387–391, 2004.
- [2] N. K. Bose and M. B. Chappalli, "A second generation wavelet framework for superresolution with noise filtering," *Intl. J. Imaging Sys. and Tech.*, vol. 14, no. 2, pp. 84–89, 2004.
- [3] J. L. Starck, E. J. Candes, and D. L. Donoho, "The curvelet transform for image denoising," *IEEE Trans. Image Processing*, vol. 11, no. 6, pp. 670–684, 2002.
- [4] J. Portilla, V. Strela, M. J. Wainwright, and E. P. Simoncelli, "Image denoising using scale mixtures of Gaussians in the wavelet domain," *IEEE Trans. Image Processing*, vol. 12, no. 11, pp. 1338–1351, 2003.
- [5] S. G. Chang, B. Yu, and M. Vetterli, "Image denoising via lossy compression and wavelet thresholding," *Proc. IEEE Intl. Conf. Image Processing*, vol. 1, pp. 604–607, 1997.
- [6] N. Moayeri and K. Konstantinides, "An algorithm for blind restoration of blurred and noisy images," Hewlett-Packard Laboratories, Technical Report: HPL-96-102, <http://www.hpl.hp.com/techreports/96/HPL-96-102.pdf>, 1996.
- [7] D. L. Donoho, "Denoising by soft thresholding," *IEEE Trans. Info. Theory*, vol. 41, no. 3, pp. 613–627, 1995.
- [8] A. Shnayderman, A. Gusev, and A. Eskicioglu, "A multidimensional image quality measure using singular value decomposition," *Proc. SPIE Image Quality and Sys. Perf. Conf.*, vol. 5294, pp. 82–92, 2004.
- [9] E. Vanraes, M. Jansen, and A. Bultheel, "Stabilised wavelet transforms for non-equispaced data smoothing," *Signal Processing*, vol. 82, no. 12, pp. 1979–1990, 2002.
- [10] Z. Wang and A. C. Bovik, "A universal image quality index," *IEEE Signal Processing Letters*, vol. 9, no. 3, pp. 81–84, 2002.
- [11] W. Sweldens, "The lifting scheme: A construction of second generation wavelets," *SIAM J. Math. Anal.*, vol. 29, no. 2, pp. 511–546, 1998.
- [12] H. Marmolin, "Subjective MSE measures," *IEEE Trans. Sys., Man, and Cybernetics*, vol. 16, no. 3, pp. 486–489, 1986.
- [13] G. W. Stewart and J. Sun, *Matrix Perturbation Theory*. Academic Press Inc., New York, 1990.
- [14] D. S. C. Biggs and M. Andrews, "Acceleration of iterative image restoration algorithms," *Applied Optics*, vol. 36, no. 8, pp. 1766–1775, 1997.

# ENHANCED BIGGS-ANDREWS ASYMMETRIC ITERATIVE BLIND DECONVOLUTION

Mahesh B. Chappalli and N. K. Bose\*

The Spatial and Temporal Signal Processing Center

Department of Electrical Engineering

The Pennsylvania State University, University Park, PA 16802

May 26, 2005

## Abstract

The main contribution of this paper is the introduction of a framework for estimation of multiple unknown blurs as well as their respective supports. Specifically, the Biggs-Andrews (B-A) multichannel iterative blind deconvolution (IBD) algorithm is modified to include the blur support estimation module and the asymmetry factor for the Richardson-Lucy (R-L) update based IBD algorithm is calculated. A computational complexity assessment of the implemented modified IBD is made. Simulations conducted on real-world and synthetic images confirm the importance of accurate support estimation in the blind superresolution problem.

**Keywords:** blind deconvolution, blur support estimation, multiframe deblurring, image sequence superresolution

---

\* *Correspondence to:* N. K. Bose; e-mail: nkb1@psu.edu

Research supported by Army Research Office Grant DAAD 19-03-1-0261.

# 1 Introduction

Blind image deconvolution involves image restoration from degraded observation(s) with either unknown or partially known information on the type and extent of the blur(s). A plethora of single channel methods have been documented in [1], [2]. Among methods that generalize from single frame (channel) blind deconvolution to the multiframe (multichannel) case is the iterative one proposed by Biggs and Andrews [3]. Multichannel blind methods that do not have single channel equivalents (however, similarities may exist as in [4]) have also been proposed [4], [5]. The subspace technique [4] is non-iterative and like other approaches, gives erroneous results for low signal-to-noise ratio (SNR) cases in comparison to iterative methods. The main advantage of the multichannel approach arises because the single channel methods are ill-posed and ill-conditioned.

A multichannel blur imaging system model may result when image acquisition is through multiple cameras as shown in Figure 1. Other possibilities leading to the same model is a consequence of image capture through multiple focuses of a single camera or images acquired from a single camera through a changing medium. Phase diversity permits restoration of target and unknown point spread function by two-channel imaging, typically in-focus and out-of-focus. There is a natural multichannel counterpart [6]. A ground-based telescope with a CCD or CMOS sensor can be used to acquire images of the spot in the solar photosphere. These images are blurred by atmospheric turbulence and refractive index fluctuation of the air caused by temperature variations.

The generic model in Figure 1 includes multichannel acquisition of an image sequence, a module for image registration based on the projective model of camera motion parameter estimation [7], [8], a module that simultaneously implements superresolution (using second generation wavelets) and noise filtering by either soft or hard thresholding [9], [10], and a module for blind blur param-

ter with support estimation that ultimately produces the deblurred, noise filtered, superresolved image. Finite support linear shift invariant blurs are reasonable to assume. The coprimeness

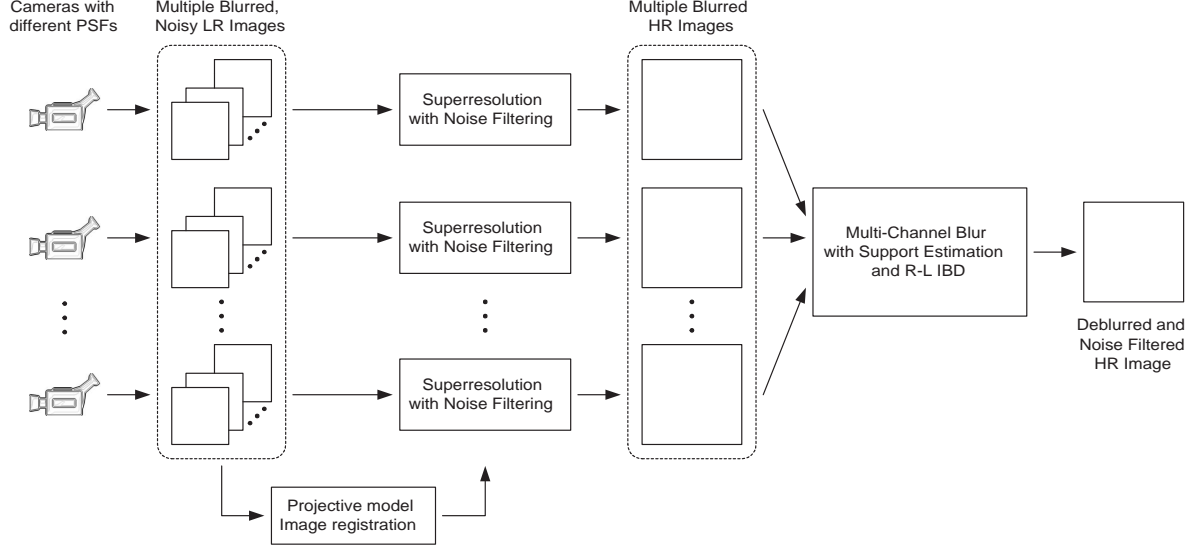


Figure 1: Multichannel Blind Superresolution Model

condition [11] on the zeros of the transfer functions representing the blurs, needed for restoration from multiple deconvolution operators, if satisfied, is expected to produce a high quality deblurred, noise filtered, superresolved image. This coprimeness condition is assumed to hold in the blind identification of multichannel finitely supported blurs in perfect two-dimensional signal restoration [12]. A multichannel high resolution blind image restoration scheme was also considered in [13]. A parameterized blur identification (when the blurring process is known only to within a set of parameters) and resolution enhancement scheme which includes restoration as a special case, has been reported in [14]. The iterative blind deconvolution (IBD) method originally proposed in [15] was extended in [3] to multiple frames using the popular Richardson-Lucy (R-L) algorithm.

The focus of this paper is on generalizing the result in [3] to include not only multiple blur identification but also support estimation of blurs that was assumed in [3] to be either known a



priori or determined by trial and error. In addition, the paper also presents a derivation for the asymmetry factor (discussed in greater depth in Section 3) required in the IBD algorithm instead of employing a trial and error approach as proposed in [3], [16]. It is also pointed out that the estimation of several unknown parameters for the problem of reconstruction of a high-resolution (HR) image from multiple under-sampled, shifted, degraded frames with subpixel displacement errors (for example, the model advanced by Bose and Boo [17]) has been considered recently in [18].

In Section 2, the multichannel point spread function with support estimation is discussed. The computational complexity of the procedure presented is analyzed and simulation results on real-world as well as synthetic data are presented. In Section 3, the asymmetry factor in the modified Biggs-Andrews (B-A) multiframe IBD is calculated for the case of interest here, i.e. procedure presented using R-L IBD algorithm instead of least-squares as previously done in [16]. In Section 4, conclusions are drawn and the new results obtained in this paper are summarized.

## 2 Multichannel PSF with Support Estimation

The resulting HR images after the superresolution step in Figure 1 still need to be deblurred for the best possible output image quality. But, in most practical cases, the blur of the acquisition system, characterized by the point spread function (PSF) is unknown. In such cases, some of the approaches that can be adopted are: the Biggs-Andrews (B-A) algorithm [3], the You-Kaveh regularization based algorithm [19] and the Kundur-Hatzinakos recursive inverse filtering algorithm [20]. Though the Kundur-Hatzinakos algorithm has the same computational complexity as the B-A algorithm, it makes several restrictive assumptions (for instance, the existence of the inverse of the original PSF) while the complexity of the You-Kaveh approach is very high. A more detailed comparison

of these and other techniques is presented in [21].

Among the three mentioned algorithms, the B-A algorithm generalizes directly to the multi-channel case. Since, in the superresolution problem, extra information in multiple high resolution frames is available, it is desirable to use a method which can exploit it for improved image quality. Hence the B-A algorithm is most suited for the multichannel case under consideration. Further, the R-L iteration, which constitutes the core of the B-A algorithm, is a form of the expectation maximization (EM) algorithm of Dempster et al. [22] (as shown by Shepp and Vardi [23]), which is an efficient and widely used image restoration algorithm. The observed image is obtained by stacking in 3-D the degraded 2-D observed images. The procedure then becomes similar to optimization algorithms where one estimates two sets of parameters in the iteration by freezing one and updating the other. A comment relevant to this type of technique (alternating minimization) is that proof of convergence is usually not feasible without appropriate conditioning, even though the convergence of the EM algorithm and hence the R-L iteration is well documented [22], [24]. However, extensive simulations have confirmed under varying conditions (high observation noise, varying blur support and initial over-estimate) that no difficulty in rapid convergence was witnessed. Instability is not an issue when using R-L iterations since it can be shown [3] that successive iterates are bounded from below by zero and from above by the total energy of the initial estimate (which is usually the observation) which is finite.

## 2.1 The Biggs-Andrews Iterative Blind Deconvolution (IBD) algorithm

The B-A IBD algorithm is an alternating variable optimization approach to estimate both the image and the PSF. It is flexible in the sense that different optimization techniques can be applied for the image and the PSF updates respectively. Further, the algorithm takes into account different

rates of convergence of the image and the PSF by allowing a different number of iterations for each within the main alternating optimization loop. This approach is termed as ‘*asymmetric IBD*’. The essence of the B-A algorithm is captured in the following figure (R-L update equations are used for both image and PSF): The basic R-L update iterations are given by the equations

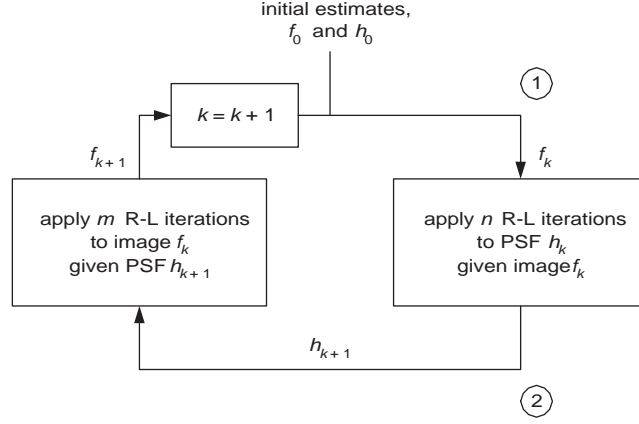


Figure 2: Biggs-Andrews (B-A) IBD algorithm

$$h_{k+1} = \frac{1}{\sum_{\Omega} f_k} h_k \cdot f_k \star \left( \frac{g}{h_k \otimes f_k} \right) \quad (1)$$

$$f_{k+1} = \frac{1}{\sum_{\zeta_k} h_{k+1}} f_k \cdot h_{k+1} \star \left( \frac{g}{h_{k+1} \otimes f_k} \right) \quad (2)$$

where  $g$  is the original observation,  $\cdot$ ,  $\star$  and  $\otimes$  represent point-wise multiplication, correlation and convolution, respectively, at every pixel location  $[i, j] \in \Omega \subset \mathbb{R}^2$ , where  $\Omega$  is the support of the image. Similarly,  $\zeta_k \subset \mathbb{R}^2$  is the support of the PSF,  $h_k$ . Acceleration and noise-dampening as described in [3] is employed in the implementation though it is not shown in the iterations described in Equations (1) and (2) above. Further details about the algorithm can be found in [3], [16]. The initial estimate of the image,  $f_0$ , is set to be equal to the observation,  $g$ . The initial estimate of the PSF,  $h_0$ , can be set to anything with the exception of zeros (one of the properties of the R-L algorithm is that zero values remain unchanged over iterations). Biggs and Andrews [3] suggest the use of the autocorrelation of the observed image as the initial estimate for the PSF. In the results

presented here, a matrix with all values equal and which sums to unity over its support is used as the initial estimate for the PSF. Termination of the iterations occurs when either the norm of the difference between successive estimates falls below a certain preset value (ex:  $10^{-3}$ ) or a maximum number of iterations (ex: 30) is reached.

**Drawback:** The biggest drawback of the above mentioned algorithm is that it requires exact knowledge of the support of the PSF for optimal performance. Thus, in a sense, it is not totally blind. Typically, since there is no information about the PSF, its support is also unknown. In [3], it is stated that when this information is unavailable, the only alternative is to over-estimate the support of the PSF (so that it contains the actual support) in order to implement the deconvolution to get the solution. This approach does not yield very good results as shown by simulation results in Section 2.3. In addition, it increases the computational complexity of the algorithm. Under-estimation of the PSF support leads to very poor deblurring.

One of the important features in the You-Kaveh algorithm is that it includes a module to iteratively achieve better estimates of the actual support of the PSF, even though, like the B-A algorithm, it also starts with an over-estimation of the support of the PSF. In order to ensure ease of practical implementation, the approach in [19] involves pruning of the PSF support such that it is always rectangular. Pruning of a boundary-constituting side  $\delta\zeta_k$  of the rectangular PSF support,  $\zeta_k$ , is carried out if

$$h_k(x) \leq T, \quad \forall x \in \delta\zeta_k \quad (3)$$

where  $T > 0$  is a threshold (the threshold should be positive since a positivity constraint is imposed on both the image and the PSF). This approach, though simple, is effective, provided a proper threshold is chosen. Various simulations presented later in this document and in [19] have shown

that this method reliably estimates the support of the PSF after a small number of iterations.

## 2.2 Enhanced Biggs-Andrews IBD with PSF Support Estimation

Since the You-Kaveh algorithm is basically designed for single channel deconvolution and better image restoration can be achieved in the superresolution problem illustrated in Figure 1 by making use of the multiple HR images, it is desirable to incorporate the iterative PSF support estimation module into the B-A algorithm. The single channel case is first considered and the generalization to the multichannel case is subsequently presented.

### 2.2.1 Single Channel PSF Support Estimation

Since the support estimation needs to be performed only on the PSF (the support of the image is known), the module can be inserted at either location “1” or location “2” marked in Figure 2 that was used to describe the B-A algorithm. The following arguments present the advantages of inserting the support pruning module at location “2” instead of location “1”:

- Consistency in the implementation of Equation 1 - the equation assumes that  $f_k$  is the image estimate when the PSF estimate is  $h_k$  which is violated to a certain degree if  $h_k$  is pruned with  $f_k$  remaining unchanged. On the other hand, insertion of the module at location “2” does not violate any of the equations. See Figure 3 for the modification of Figure 2 introduced here so that the blur support can be reliably estimated. Pruning is needed because of the initial overestimate always made.
- Initial over-estimate of the PSF support can, possibly, be reduced by a certain degree before an image update is performed

The updated depiction of the B-A algorithm is as shown in Figure 3 below. The condition for

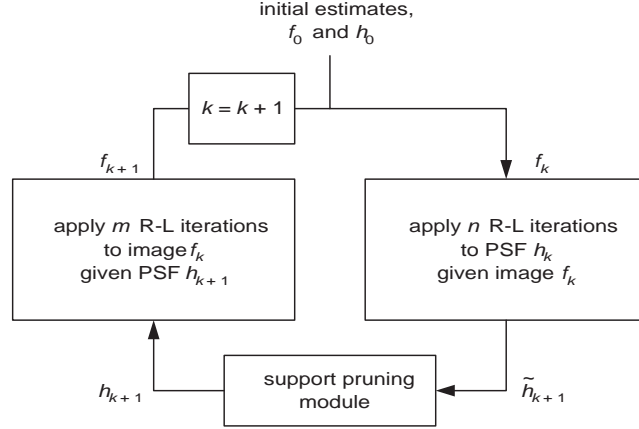


Figure 3: Modified form of the Biggs-Andrews (B-A) IBD algorithm

support pruning employed in the algorithm documented in this article is

$$\sum_{j=k-\ell}^k h_j(x) \leq T, \quad x \in \delta\zeta_k \quad (4)$$

which is similar to that employed in [19]. Here,  $h_k$  represents the current ( $k^{\text{th}}$  iteration) PSF estimate,  $T$  the threshold, and  $\delta\zeta_k$  the outermost boundary of the current PSF support,  $\zeta_k$ . The main differences with the approach in [19] are that the amount of support pruning possible in each iteration is restricted, and an option to include information about variation over the previous  $\ell$  iterations is provided. This results in the system being more robust to temporary fluctuations in the PSF estimate. The threshold,  $T$ , is heuristically set to 10% of the energy of the PSF. Thus, though the rule for the choice of the threshold is determined heuristically and is independent of the type and support of the PSF, the actual value of the threshold depends on the energy of the PSF.

### 2.2.2 Multichannel PSF Support Estimation

The single PSF case of the B-A IBD algorithm can be easily extended to the multiple PSF case.

That is, we consider imaging process given by

$$g_n = f \otimes h_n, \quad n = 1, 2, \dots, N \quad (5)$$

where  $f$  is the original image,  $g_n$  represents the  $n^{\text{th}}$  blurred observation and  $h_n$  is the corresponding PSF. To formulate this as a 3-D extension of the single channel case, it should fit into the framework of the R-L equations ((1) and (2)) which are used for alternatively updating the image and PSF estimates. Essentially, the R-L equation is an iterative maximum likelihood (ML) approach to estimate one of the terms in the RHS of

$$g = f \otimes h \quad (6)$$

given the LHS and the other term in the RHS. Hence, to extend the IBD algorithm to the multi-channel case, Equation (5) needs to be written in 3-D matrix form and 3-D versions of the operators in Equations (1) and (2) are to be used. This is easily achieved as follows:

$$g[i, j, n] = f[i, j, n] \otimes h[i, j, n], \quad n = 1, 2, \dots, N \quad (7)$$

where  $\otimes$  represents 3-D convolution. The values of  $g$  and  $h$  for fixed values of the 3<sup>rd</sup> dimension,  $n$ , represent the  $N$  blurred observations and PSFs respectively; in other words, the blurred observations and PSFs are stacked one behind the other. The signal  $f$  can now be viewed as a 3-D signal with  $f[i, j, 1]$  being the original image and with  $f[i, j, n] = 0, n = 2, 3, \dots, N$ . Thus, the R-L equation can be applied, and consequently IBD can be carried out for the multichannel case. The main difference to note is that in this case, the initial estimate for the image,  $f_0$ , and the observation,  $g$ , are not the same since the initial estimate has just one non-zero frame (to maintain the validity of Equation (7)). This is in contrast to the single channel case where the initial image estimate is, with very few exceptions, set equal to the observed image. The initial estimates of the PSF's however are set to be matrices with equal elements summing to unity, similar to the single-channel case.

The PSF support estimation module works independently on each of the PSF's and iteratively arrives at the correct support for each of the PSF's, though different number of iterations may

be required for convergence to the true support. Further, the threshold employed for support estimation will, in general, be different for each channel since the threshold is set to be 10% of the energy of the PSF. The next subsection presents simulation results which show the improvement in restoration quality achieved by the B-A algorithm with the use of the support estimation module. It also demonstrates the accuracy of the module in estimating the support of the PSF.

### 2.3 PSF Support Estimation: Simulation Results

Results for the single channel case are first presented followed by those for the multichannel case. The results show the importance and effectiveness of the iterative support estimation module. Single channel results are presented for two images: one real-world image and the other a synthetic image. Simulation results for the synthetic image for a two PSF case and a four PSF case are subsequently given. The synthetic image is designed such that it presents difficulties to the restoration algorithm (due to the very sharp contrast and transitions in the image). In a sense, it can be thought of as a stress-test for the algorithm. Also, different PSF's are used for generality.

For the results in Figures 4(b) and 4(d), the original image, PSF (support  $5 \times 5$ ) and the blurred observation are shown in Figure 4(a). The results in Figure 4(d) are generated using the original Biggs-Andrews algorithm with different guesses for the support of the PSF. As seen from the figure, over ( $9 \times 9$  and  $7 \times 7$ ) and under ( $3 \times 3$ ) estimation of the PSF support results in poor quality of restoration. Over-estimation results in inaccurate restorations - the grey squares in the original image for example, appear as white in the restoration. Under-estimation of the support size results in the output remaining significantly blurred. On the other hand, if the support of the PSF is guessed correctly/known a priori ( $5 \times 5$ ), then the original Biggs-Andrews algorithm yields good restoration results. But the support of the PSF is seldom known in blind deconvolution problems



and arriving at it by trial and error is impractical. Figure 4(b) shows the result generated for the same input using the proposed support pruning module. Though the support is initially over-estimated as  $9 \times 9$ , the algorithm iteratively arrives at the correct support as shown in Figure 4(c). It is also evident that the restored image and PSF are of very similar quality as that produced by the original Biggs-Andrews algorithm when the support is known a priori ( $5 \times 5$  case in Figure 4(d)).

Comments/inferences similar to those made above are applicable to the results presented for the real-world image in Figures 5(a), 5(b), 5(c) and 5(d). It is noted that over-estimation of the support of the PSF in the original B-A algorithm ( $13 \times 13$  and  $9 \times 9$  cases in Figure 5(d)) causes excessive ringing artifacts at the boundaries and edges while under-estimation ( $5 \times 5$  case of Figure 5(d)) results in insufficient deblurring. If the support is known a priori or arrived at by trial and error, then the best possible quality of restoration is achieved as seen from the  $7 \times 7$  case in Figure 5(d). On the other hand, if the proposed algorithm with support estimation is employed, the restoration is of good quality (Figure 5(b)) even if the support of the PSF is initially over-estimated, since the algorithm iteratively arrives at the correct support as shown in Figure 5(c).

In the multichannel cases presented subsequently, it is observed that the PSF support estimation module accurately estimates the support of the PSF in each of the channels, though the type and support of the PSF in each channel is different. Further, it is also noted that the convergence to the true support in each channel, as expected, takes different number of iterations. The quality of the restoration is also much better than in the single channel case due to the availability of more information in the form of multiple blurred observations.

Synthetic Image	checkerboard ( $64 \times 64$ pixels)
True PSF	$5 \times 5$ Gaussian with variance 10
Noise	additive white Gaussian, zero mean, variance 0.0001

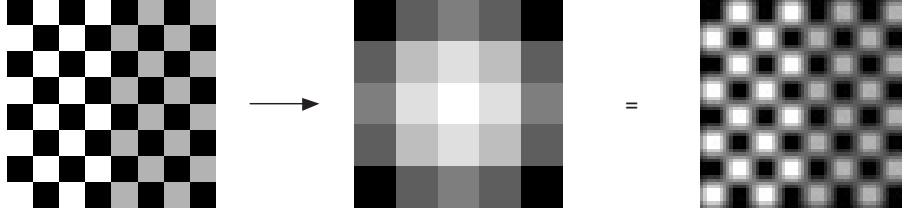


Figure 4(a): Original image, original PSF, and noisy, blurred image respectively

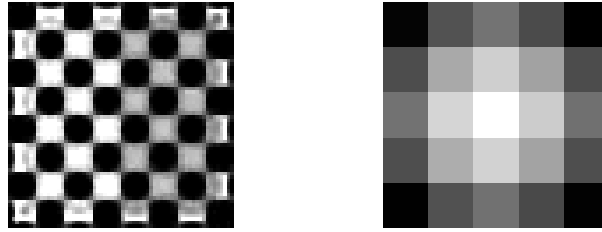


Figure 4(b): Restored image and PSF with support estimation respectively

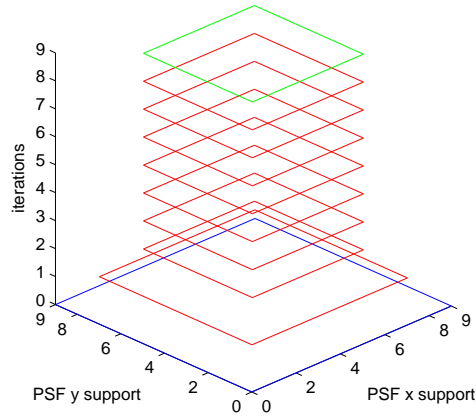


Figure 4(c): Iterative PSF support estimation (initial over-estimate:  $9 \times 9$ )

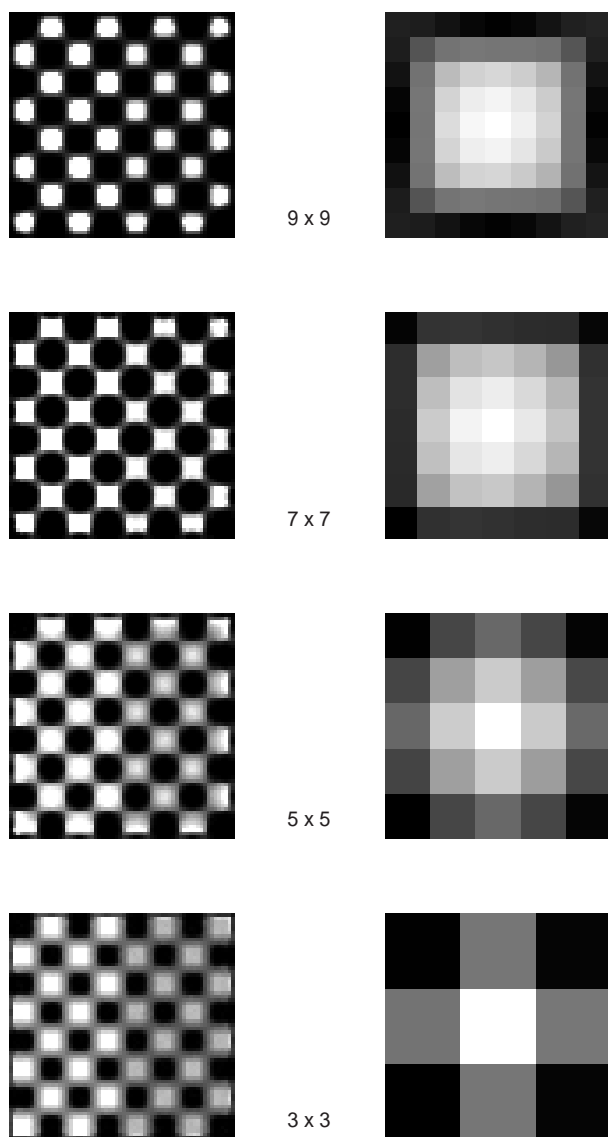


Figure 4(d): Restorations with different guesses for PSF support (without support estimation)

Real-world Image	bridge (512 $\times$ 512 pixels)
True PSF	7 $\times$ 7 Out-of-Focus/Circular
Noise	additive white Gaussian, zero mean, variance 0.0001



Figure 5(a): Original image, original PSF, and noisy, blurred image respectively



Figure 5(b): Restored image and PSF with support estimation respectively

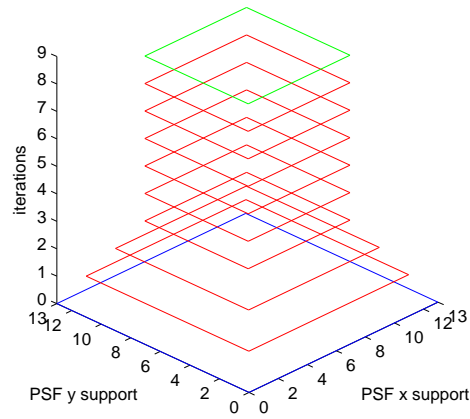
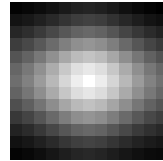
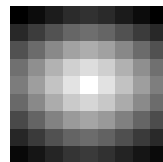


Figure 5(c): Iterative PSF support estimation (initial over-estimate:  $13 \times 13$ )



13 x 13



9 x 9



Figure 5(d): Restorations with different guesses for PSF support (without support estimation)

Synthetic Image	checkerboard ( $64 \times 64$ pixels)
True PSFs	$3 \times 3$ Gaussian with variance 10 $5 \times 5$ Out-of-Focus/Circular
Noise	additive white Gaussian, zero mean, variance 0.001

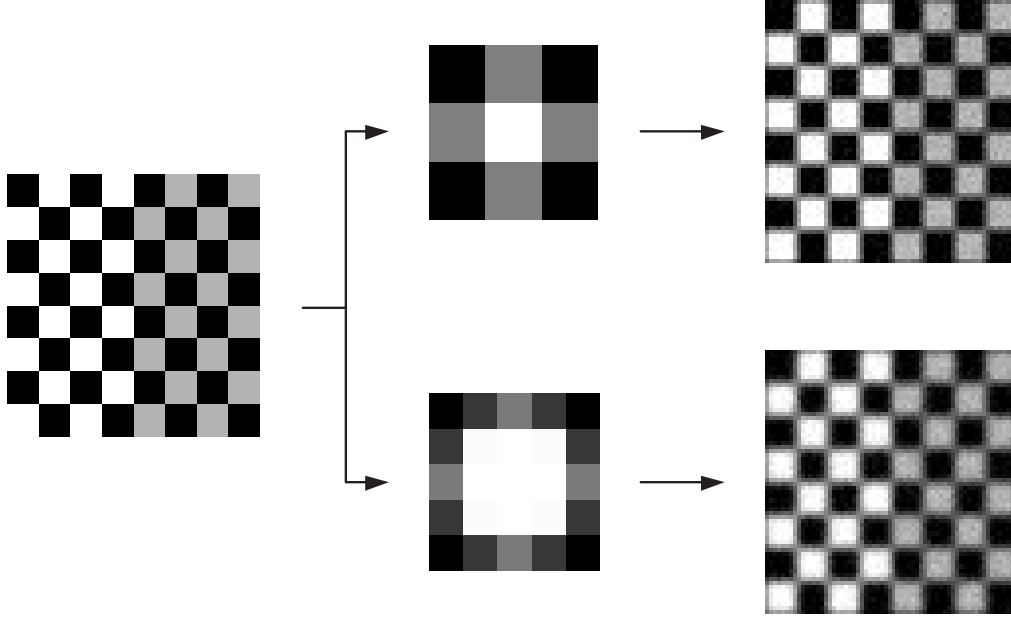


Figure 6(a): Original image, original PSFs and corresponding noisy, blurred images respectively

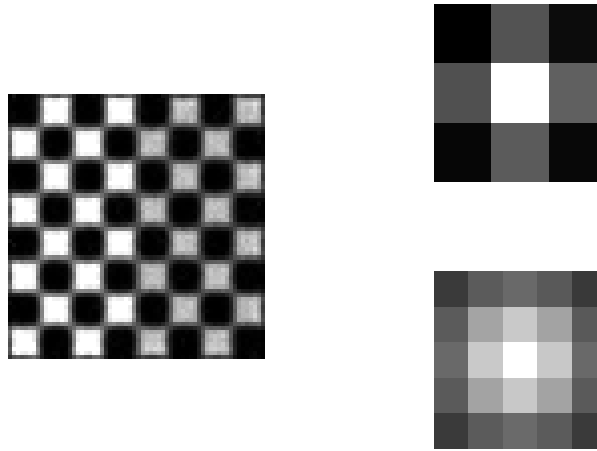


Figure 6(b): Restored image and PSFs with support estimation respectively



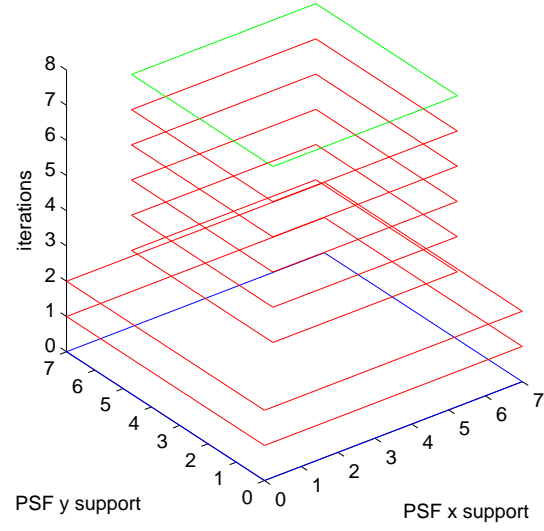
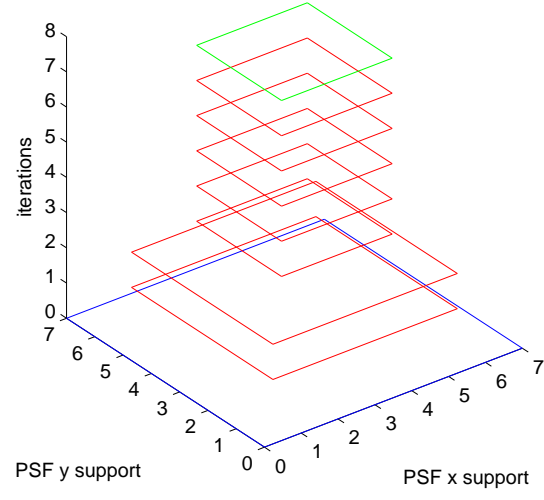


Figure 6(c): Iterative support estimates for the two restored PSFs

Synthetic Image	checkerboard ( $64 \times 64$ pixels)
True PSFs	$7 \times 7$ Gaussian with variance 10
	$5 \times 5$ Out-of-Focus/Circular
	$7 \times 7$ Gaussian with variance 2.5
	$3 \times 3$ Averaging
Noise	additive white Gaussian, zero mean, variance 0.001

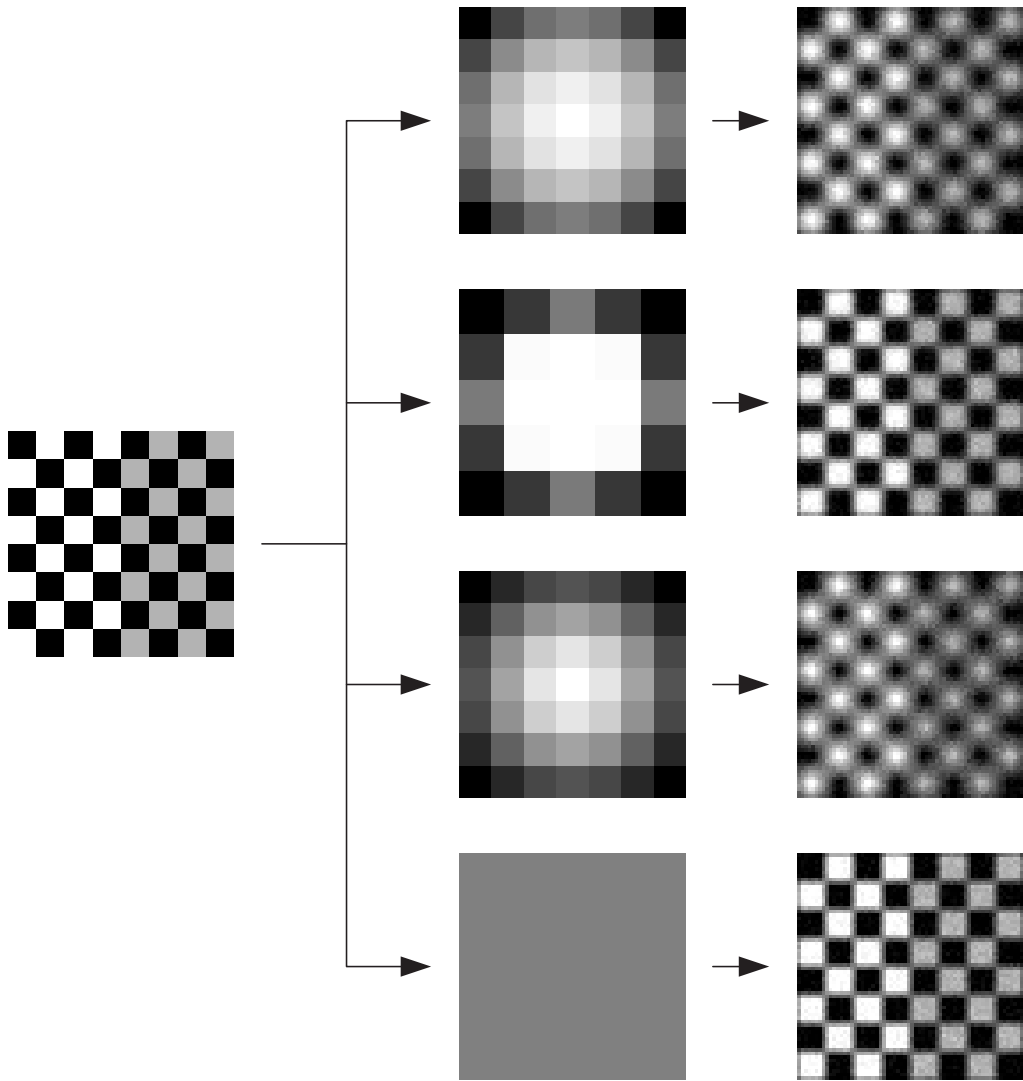


Figure 7(a): Original image, original PSFs and corresponding noisy, blurred images respectively

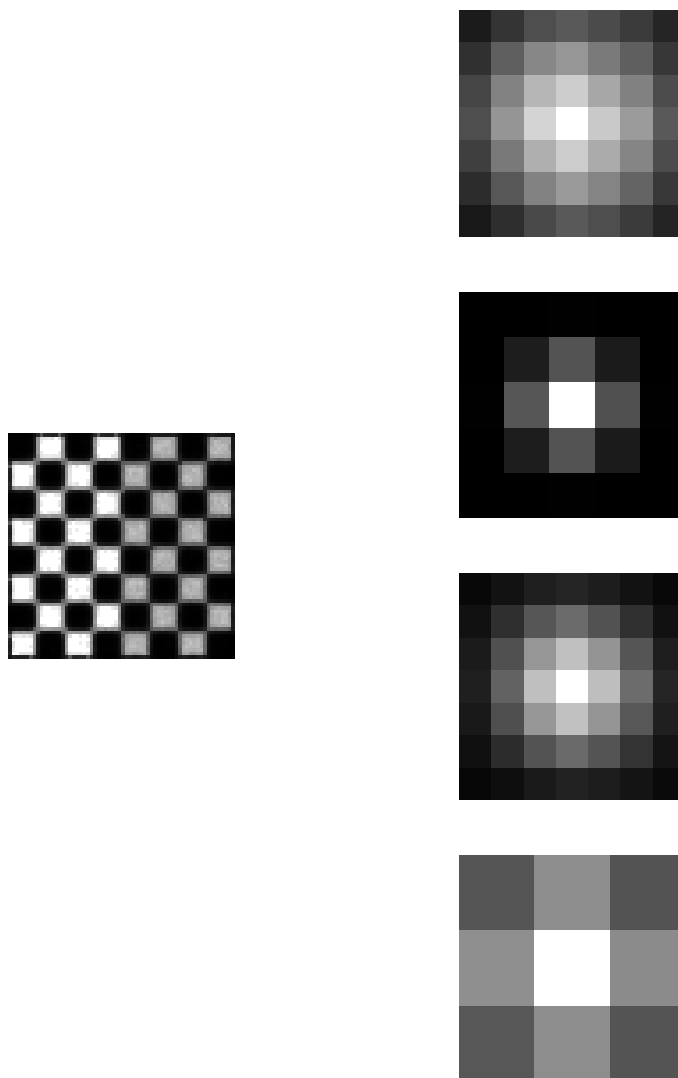
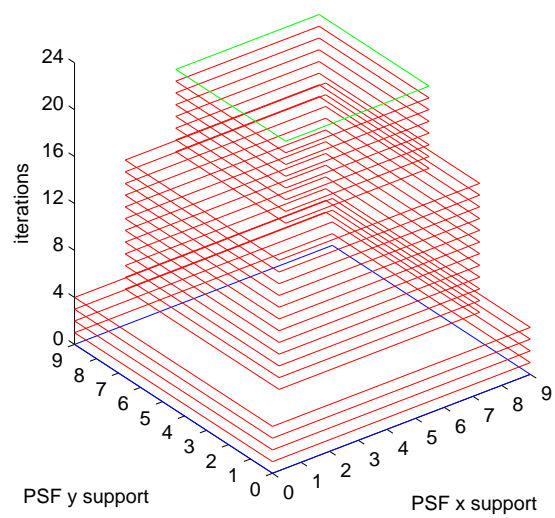
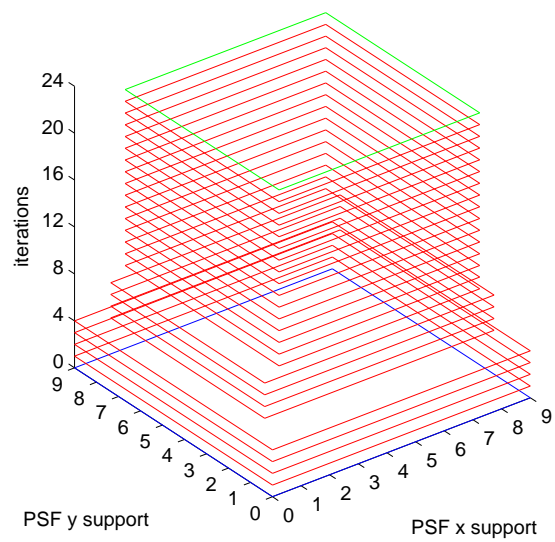


Figure 7(b): Restored image and PSFs with support estimation respectively



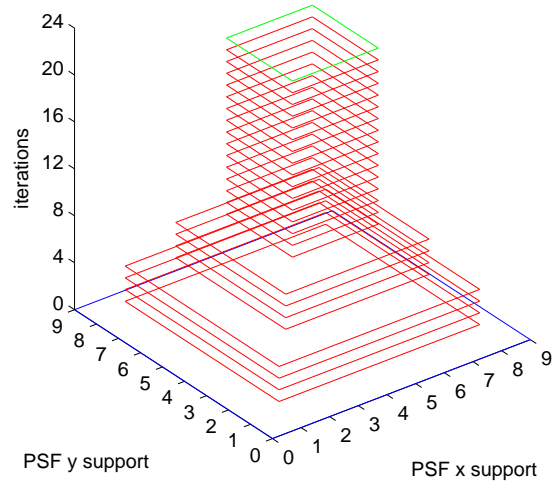
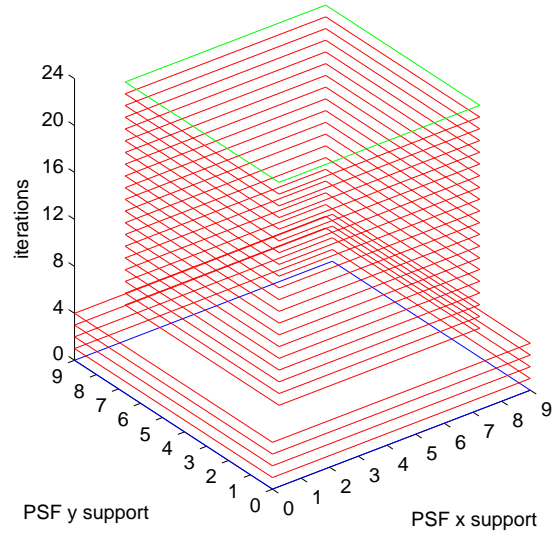


Figure 7(c): Iterative support estimates for the four restored PSFs

## 2.4 Complexity Savings due to Iterative Support Estimation

It has been shown above that the quality of the deconvolved output in the B-A algorithm is sensitive to the support of the initial guess for the PSF. The advantages of employing an iterative PSF support estimation (by pruning) similar to the You-Kaveh algorithm have also been demonstrated. In the following section, the savings in computation due to the iterative PSF support estimation module are analyzed.

The basic R-L iterations are given by Equations (1) and (2). For minimum computational complexity, the convolution and correlation operations are carried out in the Fourier domain. The above equations can then be rewritten as:

$$h_{k+1} = \frac{1}{\sum_{\Omega} f_k} h_k \cdot \mathcal{F}^{-1} \left( F_k^* \cdot \mathcal{F} \left( \frac{g}{\mathcal{F}^{-1}(H_k \cdot F_k)} \right) \right) \quad (8)$$

$$f_{k+1} = \frac{1}{\sum_{\zeta_k} h_{k+1}} f_k \cdot \mathcal{F}^{-1} \left( H_{k+1}^* \cdot \mathcal{F} \left( \frac{g}{\mathcal{F}^{-1}(H_{k+1} \cdot F_k)} \right) \right) \quad (9)$$

where  $*$  represents complex conjugation,  $\mathcal{F}$  and  $\mathcal{F}^{-1}$  represent the Fourier and inverse Fourier transform operators respectively, and  $X$  denotes the Fourier transform of the signal  $x$ .

For a real signal of length  $N$ , it can be easily shown that the computation of the Fourier transform and its inverse require  $O(N \log_2(N))$  operations. It can also be shown that the complexity of an  $n$ -dimensional Fourier transform and its inverse is the same as that of a one-dimensional signal of length equal to the product of the dimensions of the  $n$ -dimensional signal.

Assuming the image to be of size  $M \times N$  and the PSF estimate to be of size  $P \times Q$ , the complexity of implementing each of the terms in Equation (8) are listed below based on the above

paragraph and the definitions

$$\mathcal{C}(X) \triangleq C_m(X) + C_a(X)$$

$$C_m(X) \triangleq \frac{3}{2}X \log_2(X) - 5X + 8$$

$$C_a(X) \triangleq \frac{7}{2}X \log_2(X) - 5X + 8$$

where  $C_m(X)$  indicates the number of multiplications required for an  $X$ -point FFT and  $C_a(X)$  is the corresponding number of additions.

#### List of Computation Complexities

computation of $F_k$	$\mathcal{C}(MN)$
computation of $H_k$	$\mathcal{C}(MN)$
(note that the DFT of $h_k$ should be the same dimension as that of $f_k$ )	
computation of $tm_1 \triangleq \mathcal{F}^{-1}(H_k \cdot F_k)$	$\mathcal{C}(MN) + MN$
computation of $tm_2 \triangleq g/tm_1$	$MN$
computation of $tm_3 \triangleq \mathcal{F}(tm_2)$	$\mathcal{C}(MN)$
computation of $tm_4 \triangleq \mathcal{F}^{-1}(F_k^* \cdot tm_3)$	$\mathcal{C}(MN) + MN$
computation of $h_{k+1}$	$2PQ + MN$

The list for implementing Equation (9) is the same as above except for the last item on the list, whose complexity is  $2MN + PQ$ . Thus, the PSF and image update equations above have net complexities  $O(5\mathcal{C}(MN) + 4MN + 2PQ)$  and  $O(5\mathcal{C}(MN) + 5MN + PQ)$ , respectively. Further, in one iteration of the B-A algorithm, the PSF is updated  $n$  times and the image  $m$  times. Let  $K$  represent the total number of iterations of the B-A algorithm. Suppose that the support estimation routine converges to the true size of the PSF,  $\hat{P} \times \hat{Q}$ , in  $L$  iterations (for simplicity, it is assumed

that there is a dimensionality reduction of 2 in each dimension for each of the  $L$  iterations). Then, the savings in computational complexity due to the support estimation routine is

$$O\left((n+m)\left((K-L)(PQ - \hat{P}\hat{Q}) + \frac{L(L+1)}{2}(P+Q)\right)\right)$$

For the multichannel case, the savings in complexity due to the iterative support estimation determined above applies to all the PSF's (the extent of savings will naturally be different depending on the actual support of the individual PSF's).

### 3 Asymmetry Factor for R-L IBD Algorithm

The asymmetry introduced into the IBD algorithm by Biggs is an important factor deciding the quality of the deblurred output image [16]. Biggs (in [16]) derived an expression for the asymmetry factor,  $AF_k$ , for the case of the least-squares error metric based optimization approach to blind deconvolution. The derived expression was based on the approximation of the rate of convergence of the image and PSF estimates to the traces of the corresponding Hessian matrices for the error metric

$$e = \|g - h_k \otimes f_k\|^2 \tag{10}$$

The remainder of this section presents a method of computing the asymmetry factor,  $AF_k$ , for the case of the R-L IBD as an alternative to employing a trial and error based approach as suggested in [3], [16].

The metric employed here is the log-likelihood which is given by

$$\mathcal{L}(g|f_k, h_k) = \sum_{\Omega} g \log r_k - r_k \tag{11}$$

where  $r_k$  is the reblurred image at the  $k^{\text{th}}$  iteration used in the R-L update equations and is given



by

$$r_k = h_k \otimes f_k \quad (12)$$

For notational convenience, the Equation (11) is written as

$$\mathcal{L} = \sum_{x \in \Omega} g(x) \log r_k(x) - r_k(x) \quad (13)$$

where  $x$  is the 2-D coordinate  $[x_1, x_2]$  and  $\Omega \subset \mathbb{R}^2$  is the support of the image, i.e. of all of  $g, f_k$ , and  $r_k$ . Also,

$$\begin{aligned} r_k(x) &= h_k(x) \otimes f_k(x) \\ &= \sum_{t \in \zeta_k} h_k(t) f_k(x - t) \end{aligned} \quad (14)$$

where  $\zeta_k \subset \mathbb{R}^2$  is the support of the PSF  $h_k$  and  $t$  is the 2-D coordinate  $[t_1, t_2]$ . Further,  $x$  and  $t$  in the above expressions are assumed to have a lexicographical ordering. The aim now is to construct the Hessian matrices of the objective function given by Equation (11) with respect to the image and the PSF estimate. Consider the case of the image estimate first. The partial derivative of  $\mathcal{L}$  with respect to  $f_k(y)$  where  $y \in \Omega \subset \mathbb{R}^2$  is given by

$$\begin{aligned} \frac{\partial \mathcal{L}}{\partial f_k(y)} &= \frac{\partial}{\partial f_k(y)} \left( \sum_{x \in \Omega} g(x) \log r_k(x) - r_k(x) \right) \\ &= \sum_{x \in \Omega} g(x) \frac{1}{r_k(x)} \frac{\partial}{\partial f_k(y)} (r_k(x)) - \frac{\partial}{\partial f_k(y)} (r_k(x)) \\ &= \sum_{x \in \Omega} \left( g(x) \frac{1}{r_k(x)} - 1 \right) \frac{\partial}{\partial f_k(y)} (r_k(x)) \end{aligned} \quad (15)$$

(noting that  $g(x)$ , the stack of observed images, is independent of  $f_k(y)$ )

Using the definition of  $r_k(x)$  from Equation (14)

$$\begin{aligned}
\frac{\partial}{\partial f_k(y)}(r_k(x)) &= \frac{\partial}{\partial f_k(y)} \left( \sum_{t \in \zeta_k} h_k(t) f_k(x-t) \right) \\
&= \frac{\partial}{\partial f_k(y)} \left( \sum_{(x-t) \in \zeta_k} f_k(t) h_k(x-t) \right) \\
&= \begin{cases} h_k(x-y) & \text{for } (x-y) \in \zeta_k \\ 0 & \text{otherwise} \end{cases}
\end{aligned} \tag{16}$$

Hence, substituting Equation (16) in Equation (15),

$$\frac{\partial \mathcal{L}}{\partial f_k(y)} = \sum_{(x-y) \in \zeta_k} \left( \frac{g(x)}{r_k(x)} - 1 \right) h_k(x-y) \tag{17}$$

In the above derivation, the periodic boundary condition was assumed for the image. Proceeding

further, the second order partial derivative with respect to  $f_k(z)$ ,  $z \in \Omega$ , is

$$\begin{aligned}
\frac{\partial^2 \mathcal{L}}{\partial f_k(z) \partial f_k(y)} &= \frac{\partial}{\partial f_k(z)} \left( \sum_{(x-y) \in \zeta_k} \left( \frac{g(x)}{r_k(x)} - 1 \right) h_k(x-y) \right) \\
&= \sum_{(x-y) \in \zeta_k} h_k(x-y) \frac{\partial}{\partial f_k(z)} \left( \frac{g(x)}{r_k(x)} - 1 \right) \\
&= \sum_{(x-y) \in \zeta_k} h_k(x-y) g(x) \frac{\partial}{\partial f_k(z)} \left( \frac{1}{r_k(x)} \right) \\
&= \sum_{(x-y) \in \zeta_k} -h_k(x-y) g(x) \frac{1}{r_k^2(x)} \frac{\partial}{\partial f_k(z)}(r_k(x))
\end{aligned} \tag{18}$$

Using the result for the partial derivative of  $r_k(x)$  obtained in Equation (16),

$$\frac{\partial^2 \mathcal{L}}{\partial f_k(z) \partial f_k(y)} = \sum_{((x-y) \in \zeta_k) \cap ((x-z) \in \zeta_k)} -h_k(x-y) h_k(x-z) \frac{g(x)}{r_k^2(x)} \tag{19}$$

The above equation defines the Hessian matrix of the objective function given by Equation (11) with

respect to the image estimate. Due to the presence of the term  $\frac{g(x)}{r_k^2(x)}$ , the Hessian matrix generated

by the generic element in Equation (19) will, in general, not be circulant or even Toeplitz. If

$\frac{g(x)}{r_k^2(x)} = 1$  (or a constant), then the matrix is a circulant [19]. Thus, the properties of circulant

matrices cannot be exploited (as in the least-squares error case considered by Biggs in [16]) for finding the trace of the Hessian matrix. Only the diagonal elements need to be computed to find the trace of the symmetric matrix generated by the generic element in Equation (19). This corresponds to the case  $z = y$  in equation (19). Therefore,

$$\frac{\partial^2 \mathcal{L}}{\partial f_k^2(y)} = \sum_{(x-y) \in \zeta_k} -h_k^2(x-y) \frac{g(x)}{r_k^2(x)} \quad (20)$$

From the above formula, it can be seen that the RHS of Equation (20) will contain as many terms as  $\text{card}(\zeta_k)$ , the cardinality of the support of the PSF, since periodic boundary condition is assumed. Consequently, the trace of the Hessian matrix will be given by

$$\Lambda_{f_k} \triangleq \sum_{y \in \Omega} \frac{\partial^2 \mathcal{L}}{\partial f_k^2(y)} = \sum_{y \in \Omega} \sum_{(x-y) \in \zeta_k} -h_k^2(x-y) \frac{g(x)}{r_k^2(x)} \quad (21)$$

The expression for  $\Lambda_{f_k}$  given in Equation (21) contains all the elements  $\in \Omega$ . Further, with a little thought, it can be seen from Equation (21) that each element of  $\Omega$  will appear  $\text{card}(\zeta_k)$  times with each appearance being weighted by a distinct element of  $h_k$ . From this observation, the computation of the trace is relatively straightforward.

The Hessian matrix of the objective function given by Equation (11) with respect to the PSF estimate can be obtained in a similar manner as outlined above and is briefly presented below.

$$\begin{aligned} \frac{\partial \mathcal{L}}{\partial h_k(y)} &= \frac{\partial}{\partial h_k(y)} \left( \sum_{x \in \Omega} g(x) \log r_k(x) - r_k(x) \right) \\ &= \sum_{x \in \Omega} \left( g(x) \frac{1}{r_k(x)} - 1 \right) \frac{\partial}{\partial h_k(y)} (r_k(x)) \end{aligned} \quad (22)$$

Using the definition of  $r_k(x)$  from Equation (14)

$$= \begin{cases} f_k(x-y) & \text{for } y \in \zeta_k \\ 0 & \text{otherwise} \end{cases} \quad (23)$$

Hence, substituting Equation (23) in Equation (22),

$$\frac{\partial \mathcal{L}}{\partial h_k(y)} = \sum_{y \in \zeta_k} \left( \frac{g(x)}{r_k(x)} - 1 \right) f_k(x - y) \quad (24)$$

The generic element of the Hessian matrix is then obtained as

$$\begin{aligned} \frac{\partial^2 \mathcal{L}}{\partial h_k(z) \partial h_k(y)} &= \sum_{y \in \zeta_k} -f_k(x - y) g(x) \frac{1}{r_k^2(x)} \frac{\partial}{\partial h_k(z)} (r_k(x)) \\ &= \sum_{(y \in \zeta_k) \cap (z \in \zeta_k)} -f_k(x - y) f_k(x - z) \frac{g(x)}{r_k^2(x)} \end{aligned} \quad (25)$$

Again, due to the presence of the term  $\frac{g(x)}{r_k^2(x)}$ , the Hessian matrix generated by the generic element in Equation (25) will, in general, neither be circulant nor be Toeplitz. As in Equations (20) and (21), the trace,  $\Lambda_{h_k}$ , of the Hessian can be computed.

The asymmetry factor,  $AF_k$  is then computed as given by Biggs:

$$\begin{aligned} AF_k &= E_\infty \frac{\sum_{\zeta_k} h_k}{\sum_{\Omega} f_k} \cdot \frac{1}{\gamma_k} \\ \text{where} \quad \gamma_k &= \frac{|\Lambda_{f_k}|}{|\Lambda_{h_k}|} \\ \text{and} \quad E_\infty &= \frac{\sum_{\zeta_k} h^2}{\sum_{\Omega} f^2} \frac{\sum_{\Omega} f}{\sum_{\zeta_k} h} \end{aligned} \quad (26)$$

with  $f$  and  $h$  representing the original image and PSF. Since this information is unknown, an estimate of the value of  $E_\infty$  is usually employed. As stated by Biggs [16], an over estimate yields much closer performance to the optimum than an under estimate. The R-L IBD algorithm is pictorially depicted by Figure 8 (refer [16]).

### 3.1 Asymmetry Factor: Simulation Results

A simulation result is presented to compare the performance of the R-L IBD with automatic in-loop estimation of the asymmetry factor  $AF_k$ , against that of the R-L IBD with manual tuning of the

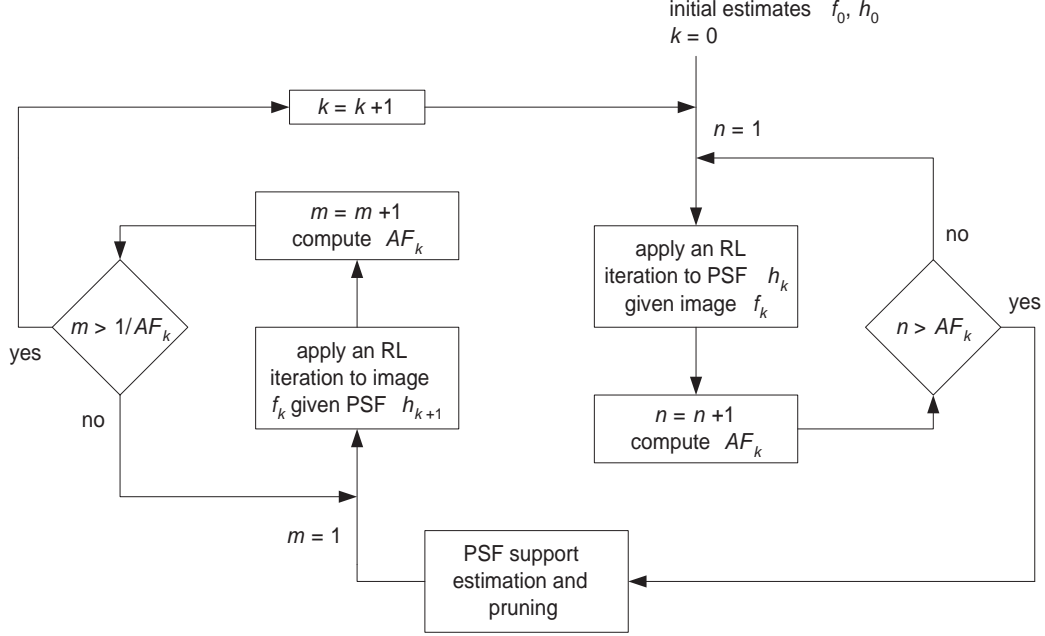


Figure 8: Modified R-L update based Asymmetric IBD algorithm

fixed asymmetry ratio. The four channel case presented earlier is considered for comparison. Figure 9 shows the restoration results for both cases, from which it is clear that the performance of the R-L IBD with automatic in-loop estimation of the asymmetry factor  $AF_k$  closely matches that of the optimally tuned R-L IBD with a fixed asymmetry ratio.

## 4 Conclusions

In the IBD algorithm shown in Figure 2, the integers  $m$  and  $n$  which are representative of the convergence rates of the image and point spread function updates, respectively, are not equal (asymmetric IBD) and the image-dependent asymmetry factor  $n/m$  was selected by trial-and-error (manual tuning). The main contributions of this paper are: first, the insertion of a support estimation (by pruning) module for each finitely supported PSF as shown in Figure 3, and, second, the computation of the asymmetry factor by finding the traces of the respective Hessian matrices whose generic elements were calculated in Equations (19) and (25). The computation of the traces, natu-

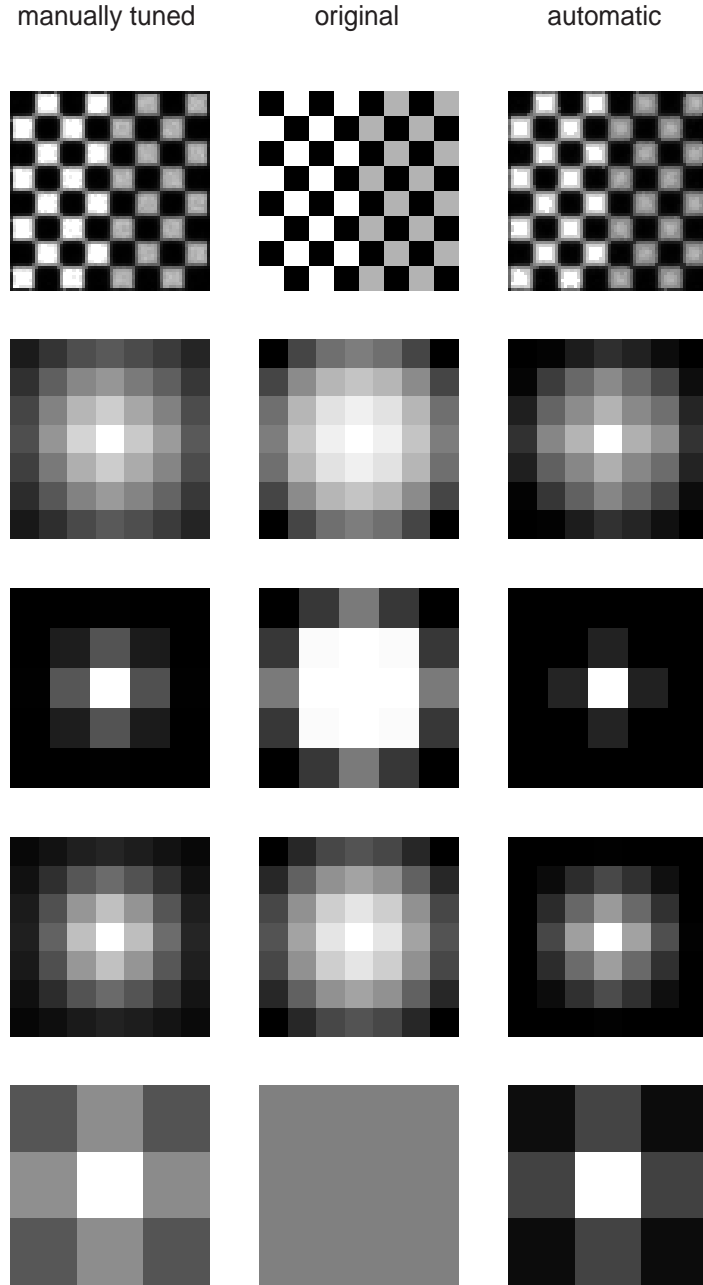


Figure 9: Restoration using R-L IBD with automatic in-loop estimation of asymmetry factor,  $AF_k$

rally, involves the finding of only the diagonal elements of these matrices, as given in Equation (20) and its counterpart that is readily derivable from Equation (25). These contributions to multiframe blind deconvolution of image sequences degraded by multiple blurs in conjunction with the already developed algorithms for superresolution and simultaneous noise filtering using second generation wavelets and thresholding [9], [10], as shown in Figure 1, will contribute significantly towards the goal of obtaining a superresolved, deblurred and noise filtered image from image sequences acquired with video cameras.

## **Acknowledgement**

The authors thank the two reviewers for their useful comments and their suggestions have been incorporated in this revised version. The support provided by Army Research Office Grant DAAD 19-03-1-0261 is gratefully acknowledged.

## References

- [1] D. Kundur and D. Hatzinakos, “Blind image deconvolution,” *IEEE Signal Processing Magazine*, vol. 13, no. 3, 1996.
- [2] M. Jiang and G. Wang, “Development of blind image deconvolution and its applications,” *Journal of X-Ray Science and Technology*, vol. 11, pp. 13–19, 2003.
- [3] D. S. C. Biggs and M. Andrews, “Asymmetric iterative blind deconvolution of multi-frame images,” *Proceedings of the SPIE Conference on Advanced Signal Processing Algorithms, Architectures, and Implementations VIII*, vol. 3461, pp. 328–338, 1998.
- [4] G. Harikumar and Y. Bresler, “Perfect blind restoration of images blurred by multiple filters: theory and efficient algorithms,” *IEEE Transactions on Image Processing*, vol. 8, no. 2, 1999.
- [5] S. U. Pillai and B. Liang, “Blind image deconvolution using a robust GCD approach,” *IEEE Transactions on Image Processing*, vol. 8, no. 2, 1999.
- [6] R. G. Paxman, T. J. Schulz, and J. R. Fienup, “Joint estimation of object and observations by using phase diversity,” *Journal of the Optical Society of America*, vol. 9, no. 7, 1992.
- [7] S. Mann and R. W. Picard, “Video orbits of the projective group: A simple approach to featureless estimation of parameters,” *IEEE Transactions on Image Processing*, vol. 6, no. 9, pp. 1281–1295, 1997.
- [8] S. Lertrattanapanich and N. K. Bose, “Latest results on high-resolution reconstruction from video sequences,” *Technical Report of IEICE, DSP99-140, The Institution of Electronic, Information and Communication Engineers, Japan*, pp. 59–65, 1999.
- [9] N. K. Bose and M. B. Chappalli, “A second generation wavelet framework for super-resolution with noise filtering,” *International Journal of Imaging Systems and Technology, Special Issue: High-Resolution Image Reconstruction I*, vol. 14, no. 2, pp. 84–89, 2004.
- [10] N. K. Bose, S. Lertrattanapanich, and M. B. Chappalli, “Super-resolution with second generation wavelets,” *Signal Processing: Image Communication*, vol. 19, no. 5, pp. 387–391, 2004.
- [11] C. A. Berenstein and E. V. Patrick, “Exact deconvolution for multiple convolution operators - an overview plus performance characterizations for imaging sensors,” *Proceedings of the IEEE*, vol. 78, no. 4, pp. 723–734, 1990.
- [12] G. B. Giannakis and R. W. Heath, “Blind identification of multi-channel FIR blurs and perfect image restoration,” *IEEE Transactions on Image Processing*, vol. 9, no. 11, pp. 1877–1896, 2000.
- [13] W. Wirawan, P. Duhamel, and H. Maitre, “Multi-channel high resolution blind image restoration,” *Proceedings of ICASSP 1999*, vol. 6, pp. 3229–3232, 1999.
- [14] N. Nguyen, P. Milanfar, and G. H. Golub, “Efficient generalized cross-validation with applications to parametric image restoration and resolution enhancement,” *IEEE Transactions on Image Processing*, vol. 10, no. 9, pp. 1299–1308, 2001.
- [15] G. Ayers and J. Dainty, “Iterative blind deconvolution method and its applications,” *Optics Letters*, vol. 13, no. 7, pp. 547–549, 1988.



- [16] D. S. C. Biggs, *Accelerated Iterative Blind Deconvolution*. PhD thesis, University of Auckland, New Zealand, 1998.
- [17] N. K. Bose and K. J. Boo, “High-resolution image reconstruction with multisensors,” *International Journal of Imaging Science and Technology*, vol. 9, no. 4, pp. 294–304, 1988.
- [18] R. Molina, M. Vega, J. Abad, and A. K. Katsaggelos, “Parameter estimation in Bayesian high-resolution image reconstruction with multisensors,” *IEEE Transactions on Image Processing*, vol. 12, no. 12, pp. 1655–1667, 2003.
- [19] Y. L. You and M. Kaveh, “A regularization approach to joint blur identification and image restoration,” *IEEE Transactions on Image Processing*, vol. 5, no. 3, 1996.
- [20] D. Kundur and D. Hatzinakos, “A novel blind deconvolution scheme for image restoration using recursive filtering,” *IEEE Transactions on Signal Processing*, vol. 46, no. 2, pp. 375–390, 1998.
- [21] M. Mignotte, J. Meunier, J. P. Soucy, and C. Janicki, “Comparison of deconvolution techniques using a distribution mixture parameter estimation: Application in single photon emission computed tomography imagery,” *Journal of Electronic Imaging*, vol. 11, no. 1, pp. 11–24, 2002.
- [22] A. D. Dempster, N. M. Laird, and D. B. Rubin, “Maximum likelihood from incomplete data via the EM algorithm,” *Journal of the Royal Statistical Society*, vol. 39, no. 1, pp. 1–38, 1977.
- [23] L. A. Shepp and Y. Vardi, “Maximum likelihood reconstruction in positron emission tomography,” *IEEE Transactions on Medical Imaging*, vol. 1, no. 2, pp. 113–122, 1982.
- [24] D. L. Snyder, T. J. Schulz, and J. A. O’Sullivan, “Deblurring subject to nonnegativity constraints,” *IEEE Transactions on Signal Processing*, vol. 40, pp. 1143–1150, 1992.

# Superresolution and Noise Filtering Using Moving Least Squares

N. K. Bose, *Life Fellow, IEEE* and Nilesh A. Ahuja

**Abstract**—An irregularly spaced sampling raster formed from a sequence of low resolution frames is the input to an image sequence superresolution algorithm whose output is the set of image intensity values at the desired high resolution image grid. The method of moving least squares (MLS) in polynomial space has proved to be useful in filtering the noise and approximating scattered data by minimizing a weighted mean square error norm, but introducing blur in the process. Starting with the continuous version of the MLS, an explicit expression for the filter bandwidth is obtained as a function of the polynomial order of approximation and the standard deviation (scale) of the Gaussian weight function. A discrete implementation of the MLS is performed on images and the effect of choice of the two dependent parameters, scale and order, on noise filtering and reduction of blur introduced during the MLS process is studied.

**Index Terms**—moving least squares, Hermite polynomials, superresolution

## I. INTRODUCTION

Most approaches to noise filtering in images, ranging from weighted least squares [1] and weighted total least squares [2] to bilateral filtering [3] assess image quality by calculating either the mean square error (MSE) or the peak signal-to-noise ratio (PSNR). Other measures of visual quality have been considered including most recently [4] a measure based on singular value decomposition ( $M_{SVD}$ ) of the image matrix, introduced first in [5]. Noise filtering with superresolution has been implemented in several approaches starting with [1] and leading upto current approaches [6]. The problem on deblurring the input blur present in low-resolution (LR) frames has been tackled in various ways [2] [7]. Post-processing has been the main recourse for input blur removal in blind superresolution, where the blurs have to be estimated. Note that the blur parameters and the respective blur supports can be estimated from the LR frames in a pre-processing step [8, and references therein], but the actual deblurring should be performed after the image fusion as a post-processing step [7], [9]. In a recent paper, the idea of implementing deblurring and interpolation simultaneously has been pursued [10] in the

case of known or a priori estimated blurs (atmospheric and camera) and an underdetermined system of linear equations that result from minimization. This underdetermined system occurs when the number of frames  $N_f < r^2$ , where  $r$  is the resolution enhancement factor along each direction. Blurs can also appear during denoising of an unblurred but noisy input. For example, in [4] and [6], the promising technique of wavelet-coefficient thresholding introduces undesirable blur necessitating the choice of an optimal threshold (the only parameter) for tradeoff between blur removal (introduced by thresholding) and noise filtering. The objective of this paper is to continue the investigation into tradeoff between the opposing effects of noise and introduced blur in other methods that apply to multiframe superresolution. The method of choice for such a study in this paper is that of (weighted) moving least squares recently used in single frame image processing [11] [12].

Moving Least Squares (MLS) is a local approximation method that has been documented in [13, Ch.4]. Here, its scope in a problem of current interest, namely superresolution, is investigated. Consider the irregularly sampled raster in Figure 1 generated by the sequence of LR frames captured by a video camera whose motion parameters may be described by the general projective model [14]. The goal of superresolution is to convert this irregularly sampled raster in Figure 1 to a regularly sampled one where this regularly sampled raster is comprised of grid points at equispaced intervals along each of the coordinate axis. The pixel value at each grid-point is computed with a polynomial approximant using the pixels in a defined neighborhood of the grid-point under consideration. Since the defined neighborhood may change from one grid-point to the next, the coefficients as well as the order of the polynomial approximant has to be adaptive. The MLS approach to superresolution, discussed here, mandates the choice of two parameters for optimal trade-off between introduced blur and noise filtering. The two parameters are the order of approximation and a scale parameter characterizing the standard deviation of the Gaussian weight function for the predictor function coefficients as described next. For an overview of various superresolution techniques, see [15].

Manuscript received June 3, 2005; revised September 18, 2005. The research reported here was conducted under the sponsorship of the National Science Foundation Grant CCF-0429481 and the Army Research Office Grant DAAD 19-03-1-0261.

N. K. Bose is with the Spatial and Temporal Signal Processing Center, Department of Electrical Engineering, The Pennsylvania State University, University Park, PA 16802 USA (e-mail: nkb@stspbk.ee.psu.edu).

Nilesh A. Ahuja is with the Spatial and Temporal Signal Processing Center, Department of Electrical Engineering, The Pennsylvania State University, University Park, PA 16802 USA (e-mail: naa136@psu.edu).

## II. CONTINUOUS MOVING LEAST SQUARES AS AN EQUIVALENT FILTERING OPERATION

For  $d$ -variate polynomial interpolation, the space of interest is the space  $\Pi_s^d$  of  $d$ -variate polynomials of total degree  $\leq s$ . Since the dimension of this polynomial space is (for a proof,

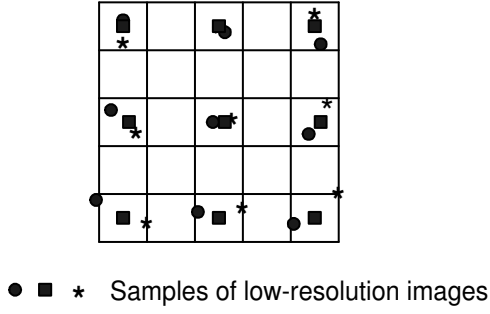


Fig. 1. Irregularly sampled raster superimposed on HR grid

see [13, pp.20-21])

$$M_s^d \triangleq \binom{s+d}{s},$$

multivariate interpolation requires the consideration of a set of sample points (nodes) of cardinality at least  $M_s^d$ . The problem of characterizing nodes that admit unique Lagrange interpolation has been extensively documented. Hermite interpolation allows coalescence of nodes along a line while coalescence of nodes along a plane gives rise to the more general Birkhoff interpolation. It is easy to show that, unlike in the univariate case, a set of distinct points may not admit a unique Lagrange interpolation in the multivariate case. For interpolation by multivariate polynomials in  $\Pi_s^d$  to be possible, the data sets have to be restricted [13, pp.19]. Due to the fundamental complexities in multivariate interpolation, it is expedient to sacrifice the global approach in favor of local surface approximation approaches as was done in [7] and the MLS approach [11] [12] for image approximation and interpolation (bivariate case). In the MLS method, the optimal fitting function is expressed as a linear combination of basis functions, whose coefficients are chosen to minimize the weighted mean squared error (MSE) between the signal and its approximant. The MSE is generated by moving the fitting function coefficient mask from position to position in the image plane. The primary difference between the approach in [11] [12] and the approach in this paper is the incorporation of a variable scale in the weight function and variable order of approximant so as to capture better the distribution of irregularly spaced samples in the problem.

To analyze the effect of the choice of scale and order on blur and noise in the reconstructed high-resolution image, a continuous formulation of MLS is used. Moreover, for the sake of simplicity, the analysis is initially carried out for a 1-D signal. The generalization to 2-D, in product separable form, is reasonably straightforward and is explained later in this section.

#### A. Analysis of 1-D Case

Here, we summarize, first, the results described by Boomgard and Weijer [11] and Fenn and Steidl [12], before deducing the formula for filter bandwidth as a function of the two parameters, scale and order. In the  $d = 1$  case, let the function

to be approximated by MLS be  $f(x)$ . Locally, about a fixed but arbitrary point  $x_0$ , the function is approximated as a linear combination of basis functions  $\phi_0(x), \phi_1(x), \dots, \phi_k(x)$ . If the basis functions are the monomials  $1, x, \dots, x^k$  respectively, then this approximation can be viewed as the truncated Taylor series expansion of  $f(x)$  about  $x = x_0$ . The approximation of  $f(x)$  about  $x = x_0$  is denoted as  $\hat{f}(x)$ . Then, the  $k$ th order approximant is,

$$\hat{f}(x) = a_0(x_0)\phi_0(x - x_0) + \dots + a_k(x_0)\phi_k(x - x_0). \quad (1)$$

The coefficients in the above expansion depend on  $x_0$ . For the sake of brevity, the argument  $x_0$  will be dropped from the notation and the coefficients will be referred to simply as  $a_i, i = 0, \dots, k$ . These coefficients are found by minimizing the weighted norm  $\|f(x) - \hat{f}(x)\|_w^2$ , which is the weighted MSE. The weighting function,  $w(x)$ , is such that the points close to the original  $x_0$  are weighted higher than the points far from  $x_0$ . Thus the approximation of  $f(x)$  by  $\hat{f}(x)$  is made local in nature by the choice of  $w(x)$ . A typical choice for  $w(x)$  (ubiquitous in adaptive system theory, e.g. [16]) is the Gaussian function

$$w(x) = \frac{1}{\sigma\sqrt{2\pi}} e^{-x^2/2\sigma^2}, \quad (2)$$

having scale (standard deviation)  $\sigma$ . From standard least-squares theory, the set of coefficients  $a_i, i = 0, \dots, k$  that minimizes the weighted MSE is the solution to the following system of linear equations [11]:

$$\begin{pmatrix} \langle f, \phi_0 \rangle_w \\ \vdots \\ \langle f, \phi_k \rangle_w \end{pmatrix} = \begin{pmatrix} \langle \phi_0, \phi_0 \rangle_w & \dots & \langle \phi_k, \phi_0 \rangle_w \\ \vdots & \ddots & \vdots \\ \langle \phi_0, \phi_k \rangle_w & \dots & \langle \phi_k, \phi_k \rangle_w \end{pmatrix} \begin{pmatrix} a_0 \\ \vdots \\ a_k \end{pmatrix}, \quad (3)$$

where,  $\langle f, \phi_i \rangle_w$  and  $\langle \phi_i, \phi_j \rangle_w$  are defined as,

$$\begin{aligned} \langle f, \phi_i \rangle_w &= \int_{-\infty}^{\infty} f(u) \phi_i(u - x_0) w(u - x_0) du \\ \langle \phi_i, \phi_j \rangle_w &= \int_{-\infty}^{\infty} \phi_i(u - x_0) \phi_j(u - x_0) w(u - x_0) du. \end{aligned}$$

Instead of the monomials  $1, x, \dots, x^k$ , scaled Hermite polynomials of order upto  $k$  can be chosen as the basis functions. The Hermite polynomial,  $H_n(x)$ , of order  $n$  is defined as

$$H_n(x) = (-1)^n e^{x^2} \frac{d}{dx} (e^{-x^2}). \quad (4)$$

Hermite polynomials upto order  $k$  span the same space as monomials upto order  $k$ , but are orthogonal with respect to the Gaussian weighting function  $w(x)$ , i.e.

$$\int_{-\infty}^{\infty} H_m(x) H_n(x) e^{-x^2} dx = \delta_{mn} 2^n n! \sqrt{\pi},$$

where  $\delta_{mn}$  is the Kronecker delta function. By choosing the basis functions as  $\phi_k(x) = H_k(x/\sigma\sqrt{2})$ , the matrix (called Gram matrix) in Eq. (3) becomes diagonal [12] and the diagonal elements are  $\|\phi_i\|_w^2 = 2^i i!$ . Using this in Eq. (3), the coefficients  $a_i, i = 0, \dots, k$  are easily shown to be

$$a_i = \frac{\langle f, \phi_i \rangle_w}{\|\phi_i\|_w^2} = \frac{\langle f, \phi_i \rangle_w}{2^i i!}. \quad (5)$$

Then, from Eq. (1),

$$\hat{f}(x) = \sum_{i=0}^k a_i \phi_i(x - x_0) = \sum_{i=0}^k \frac{\langle f, \phi_i \rangle_w}{2^i i!} \phi_i(x - x_0).$$

The equation above is an approximation of  $f(x)$ , locally around  $x = x_0$ . The value of the approximant  $\hat{f}(x_0)$  is obtained by evaluating the preceding equation at  $x = x_0$  to get

$$\hat{f}(x_0) = \sum_{i=0}^k \frac{\langle f, \phi_i \rangle_w}{2^i i!} \phi_i(0) = \left\langle f, \sum_{i=0}^k \frac{\phi_i(0) \phi_i}{2^i i!} \right\rangle_w.$$

Define

$$h(x) \triangleq \sum_{i=0}^k \frac{\phi_i(0) \phi_i(x)}{2^i i!}. \quad (6)$$

Then,

$$\begin{aligned} \hat{f}(x_0) &= \langle f, h \rangle_w = \int_{-\infty}^{\infty} f(u) h(u - x_0) w(u - x_0) du \\ &= \int_{-\infty}^{\infty} f(x_0 + u) h(u) w(u) du, \end{aligned}$$

and  $\hat{f}(x_0)$  can be obtained by linear shift-invariant filtering of  $f(x_0 + x)$  with a system characterized by the unit impulse response  $h(x)w(x)$ . It is desired to find the bandwidth of the filter whose unit impulse response is (using Eq. 6)

$$g(x) = h(x)w(x) = \sum_{i=0}^k \frac{\phi_i(0) \phi_i(x)}{2^i i!} w(x). \quad (7)$$

In the Appendix, it is proved that the bandwidth  $\Delta_\omega^2$  is explicitly computable in terms of the standard deviation  $\sigma$  and the order  $k = 2l$  or  $k = 2l + 1$  as given next

$$\Delta_\omega^2 = \frac{1}{2\sigma^2} \left[ 1 + \frac{4 \sum_{i=0}^l \sum_{j=0}^l \frac{i!2^{i+j} j!}{8^{i+j} i! j! (i+j)!}}{\sum_{i=0}^l \sum_{j=0}^l \frac{[2(i+j)]!}{8^{i+j} i! j! (i+j)!}} \right]. \quad (8)$$

Before proceeding to understand the implications of the above expression, the linear shift-invariant system theory based analysis performed in this subsection is extended to 2-D signals.

### B. Generalization to Separable 2-D

Suppose that it is desired to approximate the function  $f(\mathbf{x}) \triangleq f(x, y)$  at a point  $\mathbf{x}_0 \triangleq (x_0, y_0)$ . The function  $f(\mathbf{x})$  can be approximated locally around  $\mathbf{x}_0$  by a linear combination of the basis functions  $\phi_{ij}(\mathbf{x}) \triangleq \phi_{ij}(x, y)$ ,  $i = 1, \dots, k_1$  and  $j = 1, \dots, k_2$ . The estimate  $\hat{f}(x, y)$  about  $(x_0, y_0)$  is, therefore, expressed as,

$$\hat{f}(x, y) = \sum_{i=0}^k \sum_{j=0}^k a_{ij} \phi_{ij}(x - x_0, y - y_0), \quad (9)$$

where, without loss of generality,  $k_1 = k_2 = k$ . Like in the 1-D case, the coefficients  $a_{ij}$  are found by minimizing the weighted norm  $\|f(x, y) - \hat{f}(x, y)\|_w^2$ , where the weighting function,  $w(x, y)$ , is chosen to be product separable counterpart of Eq.

(2):

$$w(x, y) = \frac{1}{2\pi\sigma^2} e^{-(x^2+y^2)/2\sigma^2} = w(x)w(y). \quad (10)$$

The basis functions  $\phi_{ij}(x, y)$  are chosen as the bivariate Hermite polynomials  $H_{ij}(x/\sigma\sqrt{2}, y/\sigma\sqrt{2})$  in product separable form,

$$\phi_{ij}(x, y) = \phi_i(x)\phi_j(y). \quad (11)$$

The sum of the highest degrees of  $\phi_i(x)$  and  $\phi_j(y)$  chosen is the order of approximation. Here, the order of approximation is  $2k$ . The value of the function at  $\mathbf{x}_0$  is then estimated by evaluating the polynomial function in Eq. (9) at  $\mathbf{x} = \mathbf{x}_0$ . Similar to Eq. (5), the coefficients  $a_{ij}$  can be found as

$$a_{ij} = \frac{\langle f, \phi_{ij} \rangle_w}{\|\phi_{ij}\|_w^2}. \quad (12)$$

Using Eq. (12) in Eq. (9) results in

$$\hat{f}(x, y) = \sum_{i=0}^k \sum_{j=0}^k \langle f, \phi_{ij} \rangle_w \frac{\phi_{ij}(x - x_0, y - y_0)}{\|\phi_{ij}\|_w^2}$$

which, evaluated at  $(x, y) = (x_0, y_0)$  yields,

$$\begin{aligned} \hat{f}(x_0, y_0) &= \sum_{i=0}^k \sum_{j=0}^k \langle f, \phi_{ij} \rangle_w \frac{\phi_{ij}(0, 0)}{\|\phi_{ij}\|_w^2} \\ &= \left\langle f, \sum_{i=0}^k \sum_{j=0}^k \frac{\phi_{ij}(0, 0) \phi_{ij}}{\|\phi_{ij}\|_w^2} \right\rangle_w. \end{aligned} \quad (13)$$

Again, as in the 1-D case of Eq. (7), the equivalent filter unit impulse response is

$$g(x, y) = \sum_{i=0}^k \sum_{j=0}^k \frac{\phi_{ij}(0, 0) \phi_{ij}(x, y)}{\|\phi_{ij}(x, y)\|_w^2} w(x, y). \quad (14)$$

Using the separability of the basis functions and the weight function, the above expression simplifies to

$$\begin{aligned} g(x, y) &= \left( \sum_{i=0}^k \frac{\phi_i(0) \phi_i(x)}{\|\phi_i(x)\|_w^2} w(x) \right) \left( \sum_{j=0}^k \frac{\phi_j(0) \phi_j(y)}{\|\phi_j(y)\|_w^2} w(y) \right) \\ &\triangleq g_1(x)g_2(y), \end{aligned} \quad (15)$$

where  $g_1(x)$  and  $g_2(y)$  are the summations in the respective brackets. The 2-D Fourier transform (FT) of  $g(x, y)$  is

$$\begin{aligned} G(\omega_1, \omega_2) &= \int_{-\infty}^{\infty} \int_{-\infty}^{\infty} g_1(x)g_2(y) e^{-j(\omega_1 x + \omega_2 y)} dx dy \\ &= \left( \int_{-\infty}^{\infty} g_1(x) e^{-j\omega_1 x} dx \right) \left( \int_{-\infty}^{\infty} g_2(y) e^{-j\omega_2 y} dy \right) \\ &\triangleq G_1(\omega_1)G_2(\omega_2), \end{aligned} \quad (16)$$

where  $G_1(\omega_1)$  and  $G_2(\omega_2)$  are the integrals in the respective brackets. Finally, the radial bandwidth of this filter is

$$\begin{aligned} \Delta_{\omega_1, \omega_2}^2 &= \frac{\int_{-\infty}^{\infty} \int_{-\infty}^{\infty} (\omega_1^2 + \omega_2^2) |G(\omega_1, \omega_2)|^2 d\omega_1 d\omega_2}{\int_{-\infty}^{\infty} \int_{-\infty}^{\infty} |G(\omega_1, \omega_2)|^2 d\omega_1 d\omega_2} \\ &= \Delta_{\omega_1}^2 + \Delta_{\omega_2}^2, \end{aligned}$$

where,

$$\begin{aligned}\Delta_{\omega_1}^2 &= \frac{\int_{-\infty}^{\infty} \int_{-\infty}^{\infty} \omega_1^2 |G_1(\omega_1)|^2 |G_2(\omega_2)|^2 d\omega_1 d\omega_2}{\int_{-\infty}^{\infty} \int_{-\infty}^{\infty} |G_1(\omega_1)|^2 |G_2(\omega_2)|^2 d\omega_1 d\omega_2} \\ &= \frac{\int_{-\infty}^{\infty} \omega_1^2 |G_1(\omega_1)|^2 d\omega_1}{\int_{-\infty}^{\infty} |G_1(\omega_1)|^2 d\omega_1}.\end{aligned}$$

and  $\Delta_{\omega_2}^2$ , is defined likewise. Thus, the 1-D result is sufficient to evaluate the separable 2-D case too.

### C. Inferences

The analysis of the previous two subsections shows that the MLS technique can be viewed as a filtering operation. An expression for the bandwidth of this filter is given in Eq. (8). The following observations can be made from this expression:

- 1) An increase in scale causes a decrease in bandwidth and vice versa. This result is intuitively appealing since a larger scale means that the support of the weighting function  $w(x)$  and hence of the filter unit impulse response  $g(x)$  is larger, which causes greater averaging or smoothing (blurring). In the frequency domain, this is equivalent to a reduction in bandwidth, which produces more noise filtering.
- 2) The expression for dependence on order is seemingly complicated. A plot of filter bandwidth at a fixed scale versus the order, described in Eq. (8), is shown in Figure 2. The plot shows that bandwidth increases approximately linearly with filter order. This is not surprising either since by using a higher order, rapid changes (or high-frequency components) in the original signal can be modelled more accurately. Again, in frequency domain terms, this is equivalent to an increase in bandwidth that admits more noise.

For image sequence superresolution, the above two effects result in a tradeoff between noise in the reconstructed image and the blur introduced by the MLS process. Increasing scale lowers the bandwidth of the filter resulting in greater noise filtering but more output blur. Increasing order increases the bandwidth of the filter thereby reducing the blur introduced by the process at the expense of increased noise in the reconstructed image.

## III. MLS APPLIED TO IMAGE SUPERRESOLUTION

In image superresolution, the input is known at a set of irregularly spaced discrete data points generated from a sequence of registered LR frames and the aim is to estimate the image intensity on the regularly sampled raster of the HR grid. For this, a discrete implementation of the MLS procedure is used. In this section, the discrete formulation of MLS is explained, its similarity to local polynomial regression in statistics is pointed out and a technique to adaptively select the scale and order parameters for estimating the image intensity at each point of the HR grid is described.

### A. Discrete MLS

Given the samples of a function  $f(\mathbf{x}) \triangleq f(x_1, x_2)$  at  $N$  points  $\mathbf{x}_m \triangleq (x_{m1}, x_{m2}), m = 1, \dots, N$ , it is de-

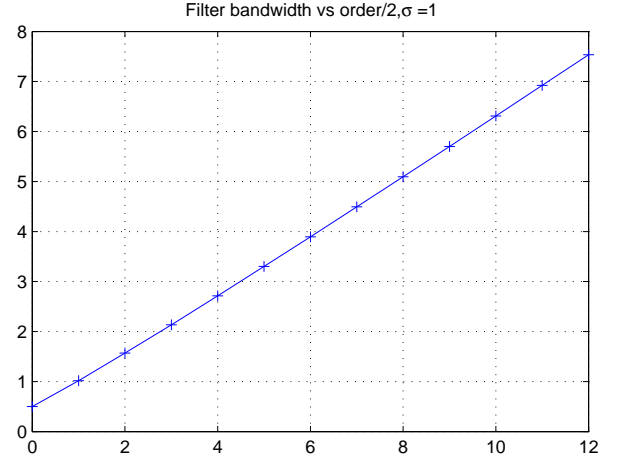


Fig. 2. Filter bandwidth vs order/2

sired to estimate the value of the function at some arbitrary but fixed point  $\mathbf{x}_0$ . Locally about  $\mathbf{x}_0$ , the function is expressed a linear combination of basis functions  $\phi_0(\mathbf{x}), \phi_1(\mathbf{x}), \dots, \phi_k(\mathbf{x})$ . If the basis functions are the bivariate monomials  $1, x_1, x_2, x_1^2, x_1x_2, x_2^2, \dots$ , etc., then this can be viewed as the Taylor series expansion of  $f(\mathbf{x})$  about  $\mathbf{x} = \mathbf{x}_0$ . Denote the approximation of  $f(\mathbf{x})$  about  $\mathbf{x} = \mathbf{x}_0$  by  $\hat{f}(\mathbf{x})$ . Then,

$$\hat{f}(\mathbf{x}) = a_0\phi_0(\mathbf{x} - \mathbf{x}_0) + \dots + a_k\phi_k(\mathbf{x} - \mathbf{x}_0). \quad (17)$$

The coefficients  $a_i, i = 0, \dots, k$  are found by minimizing the weighted norm  $\|f(\mathbf{x}) - \hat{f}(\mathbf{x})\|_w^2$ , where the weight function  $w(\mathbf{x}) \triangleq w(x_1, x_2)$  is chosen to be the circularly symmetric bivariate Gaussian function given by

$$w(\mathbf{x}) = \frac{1}{2\pi\sigma^2} e^{-\|\mathbf{x}\|^2/2\sigma^2}, \|\mathbf{x}\|^2 = x_1^2 + x_2^2. \quad (18)$$

This results in a system of linear equations similar to the one in (3). However, the weighted inner-product and the weighted norm are now defined differently as

$$\begin{aligned}\langle \phi_i, \phi_j \rangle_w &= \sum_{m=1}^N \phi_i(\mathbf{x}_m - \mathbf{x}_0) \phi_j(\mathbf{x}_m - \mathbf{x}_0) w(\mathbf{x}_m - \mathbf{x}_0) \\ &= \Phi_i^T \mathbf{W} \Phi_j\end{aligned} \quad (19)$$

$$\begin{aligned}\|\phi_i\|_w^2 &= \sum_{m=1}^N |\phi_i(\mathbf{x}_m - \mathbf{x}_0)|^2 w(\mathbf{x}_m - \mathbf{x}_0) \\ &= \Phi_i^T \mathbf{W} \Phi_i,\end{aligned} \quad (20)$$

where,

$$\Phi_i = [\phi_i(\mathbf{x}_1 - \mathbf{x}_0) \dots \phi_i(\mathbf{x}_N - \mathbf{x}_0)]^T \quad (21a)$$

$$\mathbf{W} = \text{diag}(w(\mathbf{x}_1 - \mathbf{x}_0), \dots, w(\mathbf{x}_N - \mathbf{x}_0)). \quad (21b)$$

Thus, the counterpart of Eq. (3) for discrete MLS can be compactly represented as

$$\Phi^T \mathbf{W} \mathbf{f} = \Phi^T \mathbf{W} \Phi \mathbf{a}, \quad (22)$$

where,

$$\Phi = [\Phi_0 \dots \Phi_k], \quad \mathbf{f} = \begin{pmatrix} f(\mathbf{x}_1) \\ \vdots \\ f(\mathbf{x}_N) \end{pmatrix}, \quad \mathbf{a} = \begin{pmatrix} a_0 \\ \vdots \\ a_k \end{pmatrix},$$

and the solution of the system is, therefore, given by

$$\mathbf{a} = (\Phi^T \mathbf{W} \Phi)^{-1} \Phi^T \mathbf{W} \mathbf{f}, \quad (23)$$

where the inverse of  $\Phi^T \mathbf{W} \Phi$  exists under mild constraints on the number  $N$  and distribution of the irregularly spaced points about  $\mathbf{x}_0$ . The above technique is closely related to that of *local polynomial regression* found in computational statistics [17]. Local regression is used to model a relation between a predictor variable  $\mathbf{x}$  and a response variable  $y$  related to the predictor variable. Suppose a dataset consists of  $N$ -pairs of observations,  $(\mathbf{x}_1, y_1), \dots, (\mathbf{x}_N, y_N)$ . A model of the form

$$y_m = \mu(\mathbf{x}_m) + \epsilon_m \quad (24)$$

is assumed where  $\mu(\mathbf{x})$  is an unknown function and  $\epsilon_m$  is an error term representing the random errors in the observations. The errors  $\epsilon_m$  are assumed to be independent and identically distributed, i.e. the covariance matrix of the errors is  $\sigma_n^2 \mathbf{I}$  where  $\sigma_n^2$  is the variance of each of the error terms. Locally, around a point  $\mathbf{x}_0$ , it is assumed that  $\mu(\mathbf{x})$  can be well approximated by  $\hat{\mu}(\mathbf{x})$  in terms of its Taylor series expansion up to a certain order  $k$ , i.e.

$$\hat{\mu}(\mathbf{x}) = a_0 \phi_0(\mathbf{x} - \mathbf{x}_0) + \dots + a_k \phi_k(\mathbf{x} - \mathbf{x}_0),$$

where  $\phi_0(\mathbf{x}), \phi_1(\mathbf{x}), \phi_2(\mathbf{x}), \dots$  are the bivariate monomials  $1, x_1, x_2, \dots$  respectively. By following a weighted least squares technique similar to the one used for discrete MLS, an expression similar to the one given in Eq. (23) can be arrived at for the coefficients by replacing  $\mathbf{f}$  in Eq. (23) by the observation vector  $\mathbf{y} \triangleq [y_1 \dots y_N]^T$ . The estimate at  $\mathbf{x} = \mathbf{x}_0$  is then evaluated to be

$$\begin{aligned} \hat{y}_0 &= \hat{\mu}(\mathbf{0}) = [\phi_0(\mathbf{0}) \dots \phi_k(\mathbf{0})] \mathbf{a} \\ &= [1 \ 0 \ \dots \ 0] (\Phi^T \mathbf{W} \Phi)^{-1} \Phi^T \mathbf{W} \mathbf{y}. \end{aligned} \quad (25)$$

Two important measures of the quality of this estimator are its bias and its variance, which are defined as follows

- Bias( $\hat{y}_0$ ) =  $E\{\hat{y}_0\} - y_0$ .
- Variance =  $E\{(y_0 - E\{\hat{y}_0\})^2\}$ .

These measures are controlled by the two parameters used in the regression procedure:

- 1) the scale of the weighting function, also referred to as *bandwidth* in the statistics literature (not to be confused with the bandwidth of the filter  $G(\omega)$  obtained in subsection II-A), and
- 2) the order of the truncated Taylor series expansion.

Both these parameters have a critical effect on the local regression fit. If the scale is too small, insufficient data will fall within the chosen support of the weight function and a large variance, or a noisy fit will result. On the other hand, if the scale is too large, the local polynomial may not fit the data well within the window of the weight function, resulting in a larger bias. This is especially true in regions where the

data changes rapidly or has large curvature. The order of approximation has the opposite effect on bias and variance. A higher order of approximation means that the estimate fits the data well, resulting in a lower bias. However, since the number of unknowns (coefficients) involved in this is larger, the variance of the estimate is higher. Thus, these two parameters must be chosen to compromise this bias-variance tradeoff.

In image superresolution, variance is a measure of the noise in the output and bias is a measure of the amount of blur introduced by the MLS process. Thus, a technique is needed that would permit selection of the scale and order locally so that an effective compromise between blur introduced by the process and noise in the output is reached. This is really a model selection problem which has been explored extensively in the statistics and signal processing literature. One possible solution is described in the next subsection.

### B. Selecting Scale And Order: Model Selection Criteria

In order to evaluate the effect of scale and order selection on the estimated value, it is required to define a criterion that assess the performance of the fit. Using mean square error (MSE) as a criterion is not advisable, as the estimator that fits the noisy data perfectly would then be the best estimator, which is clearly not desired. The desired criterion should indicate poor performance in case of both high bias and high variance situations. Two commonly used criteria are mentioned below [17]:

- 1) Prediction mean square error (PMSE) is defined as

$$PMSE = E\{(y_{new} - \hat{\mu}(\mathbf{x}_{new}))^2\}.$$

PMSE measures the quality of prediction. However, since we have only one set of data, an estimate of the PMSE is implemented by the cross validation (CV) estimator [18] which is defined as

$$CV = \frac{1}{N} \sum_{m=1}^N (y_m - \hat{\mu}_{-m}(\mathbf{x}_m))^2,$$

where  $\hat{\mu}_{-m}(\mathbf{x}_m)$  denotes the estimate of  $\mu(\mathbf{x}_m)$  obtained by leaving out  $\mathbf{x}_m$  and computing it from the remaining  $N - 1$  points. A lower value of  $CV$  indicates a better fit.

- 2) The scaled sum of squared error (SSE) is defined as

$$SSE = \frac{1}{\sigma_n^2} \sum_{m=1}^N (\mu(\mathbf{x}_m) - \hat{\mu}(\mathbf{x}_m))^2.$$

Note that this is different from MSE, which is  $\sum_m (y_m - \hat{\mu}(\mathbf{x}_m))^2$ . It attempts to measure how accurately the estimate  $\hat{\mu}(\mathbf{x}_m)$  approximates  $\mu(\mathbf{x}_m)$ , instead of measuring how well the estimated points  $\hat{\mu}(\mathbf{x}_m)$  fit the data  $y_m$ . The  $C_p$  criterion provides an unbiased estimate of the  $SSE$  and is given by [19]

$$C_p = \frac{1}{\sigma_n^2} \sum_{m=1}^N (y_m - \hat{\mu}(\mathbf{x}_m))^2 - N + 2p, \quad (26)$$

where  $p$  is the number of parameters in the model. Since the model used here has coefficients  $a_0, \dots, a_k$ , therefore,  $p$  is equal to  $k+1$ . A low value of  $C_p$  indicates a better fit. It should also be noted that  $C_p$  criterion is a modified version of the AIC criterion developed by Akaike several years back and used recently in [20].

For evaluation, the  $C_p$  metric requires much fewer computations than the  $CV$  metric. Thus, in the simulations and results that follow, the  $C_p$  criterion will be used for selection of model parameters. Before proceeding further, it should be noted that the expression for  $C_p$  given in Eq. (26) is actually valid for “global” regression techniques. For local regression involving the Gaussian weight function used here, the definition needs to be modified to [21]

$$C_p = \frac{1}{\text{tr}(\mathbf{W})} \sum_{m=1}^N \frac{w_m}{\sigma_n^2} (y_m - \hat{\mu}(\mathbf{x}_m))^2 - 1 + 2 \frac{\text{tr}(\mathbf{M}_2)}{\text{tr}(\mathbf{W})}, \quad (27)$$

where,

$$\mathbf{M}_2 = (\Phi^T \mathbf{W} \Phi)^{-1} \Phi^T \mathbf{W}^2 \Phi,$$

and  $\mathbf{W}$  is the diagonal matrix in Eq. (21b) involving the weights  $w_m \triangleq w(\mathbf{x}_m - \mathbf{x}_0)$ . Note that the expression for the localized  $C_p$  requires an estimate of the noise variance  $\sigma_n^2$ . The variance of the intensity values in a region of the image that does not contain any sharp edges or rapid repetitive variations (textures) is estimated. For regions that are fairly constant in the original image, this variance can almost entirely be attributed to the noise.

### C. Computational complexity

One of the advantages of using local regression methods such as MLS is that they involve solving a large number of small system of equations as against a single large system usually required by global approaches. An analysis of the computational complexity of MLS is provided in [13], [22]. It is shown in [22] that the complexity of the approximant at a single point  $x$  is bounded by  $O(Q^3 + Q^2|I(x)| + Q|I(x)|)$ , where  $Q$  is the dimensionality of the polynomial space and  $|I(x)|$  is the number of points in the neighborhood  $I(x)$  of the point  $x$  used in the computation. Clearly,  $Q$  and  $|I(x)|$  depend, respectively, on the order and scale parameters.

This bound is valid for a fixed scale and order. In the adaptive approach, it is desired precisely to find a scale and order that would result in the optimal tradeoff between blur and noise. Thus, statistical techniques have been adopted to adaptively choose the scale and order for each point. One of the techniques which involves the  $C_p$  metric has been described here. Due to the complex interdependency between scale and order, there is, so far, no known technique that can search simultaneously for the optimal scale and order. The usual practice is to fix one of the parameters and optimize for the other and repeat this process for different values of the first parameter. This is, obviously, a more computation intensive process than the simple MLS process using fixed scale and order, since it involves repeating the process for different values of scales and orders. The number of computations performed can be limited by restricting the range

of scale and order values over which the search is done. The justification behind this is that real images can usually be well approximated by piecewise polynomials of orders less than five, and it makes no sense to choose the scale value so large that points very far away from the point being estimated end up being used in the computation. This is especially true in the MLS approach, where the weight function  $w(x)$ , ideally, vanishes for arguments  $x = x_1$  and  $x = x_2$  with  $\|x_1 - x_2\|$  greater than a certain threshold [13, pp.35]. There exist several other technical devices to speed up computations. These are based on the idea that scale should be a smooth function of the point  $x$  being approximated [13, pp.43] and the order needs to be chosen from a set of low cardinality. Thus, instead of evaluating the scale and order at all desired points, these can be evaluated for a smaller set of points. The value of the scale and order at other points can be obtained by interpolating the values obtained for the smaller set. Details on methods to implement such techniques efficiently can be found in [20] [23].

## IV. SIMULATION RESULTS

Simulation results demonstrating some of the important properties of MLS and its application to superresolution are presented here. Both synthetic and real images are considered. The PSNR and  $M_{SVD}$  metrics are used as indicators of performance. The  $M_{SVD}$  metric, defined in [5], is based on the singular values of the image and gives a much better representation of the quality of an image with regard to the human visual system for a large variety of distortions. The  $M_{SVD}$  metric has also been used in the context of second-generation wavelet superresolution [4] [6] to choose a threshold value for the wavelet coefficients that strikes an optimal balance between noise filtering and blur introduced by the thresholding. A lower value of  $M_{SVD}$  indicates better image visual quality.

Figure 3 shows four LR frames of size  $64 \times 64$  of the synthetic “cameraman” image corrupted by noise of variance 0.01. The desired resolution enhancement factor is 2; hence the resulting HR images are  $128 \times 128$ . The HR images obtained by choosing a fixed scale and order for the entire image, along with their corresponding PSNR and  $M_{SVD}$  metrics are shown for different values of scales and orders in Figures 4 and 5. The tradeoff between blur (bias) and noise (variance) described in subsection II-C can be clearly seen from these images. The HR image obtained by adaptively selecting the scale and order is shown in Figure 6. Even though the image obtained by the adaptive procedure does not have the highest PSNR, or the lowest  $M_{SVD}$ , certain distinctive features in the image such as the leg of the tripod and the building in the background are captured much better in the adaptive mode of image reconstruction than in any of the fixed scale and order modes.

Next, the results obtained by using MLS in superresolution are compared to those obtained by the surface approximation method based on Delaunay triangulation [7]. Figure 7(a) shows one sample from the six  $64 \times 64$  size LR frames of the tank image sequence, corrupted by noise of variance 0.005. Here



Fig. 3. Four LR Frames of the cameraman image sequence.



Fig. 4. Reconstructed images with approximation orders 0,2,4 for a fixed value of scale; (a) Scale=0.4, Order=0, PSNR=22.78,  $M_{SVD}$ =0.08; (b) Scale=0.4, Order=2, PSNR=23.07,  $M_{SVD}$ =0.05; (c) Scale=0.4, Order=4, PSNR=20.25,  $M_{SVD}$ =0.16



Fig. 5. Reconstructed images with different chosen scales for a fixed order of approximation; (a) Scale=0.4, Order=4, PSNR=20.25,  $M_{SVD}$ =0.16; (b) Scale=0.6, Order=4, PSNR=22.93,  $M_{SVD}$ =0.06; (c) Scale=0.8, Order=4, PSNR=23.53,  $M_{SVD}$ =0.05

again, the resolution enhancement factor is 2. The resulting HR image obtained from the Delaunay triangulation method is shown in Figure 7(b) and that obtained from the MLS technique is shown in 7(c). It is seen that owing to the adaptive nature of MLS, it performs better in filtering noise while at the same time preserving edges.

Finally, the result of applying the Moving Least Squares method to a real data sequence (supplied by Air Force Research Laboratory at Rome, NY) is shown next. Figure 8(a) shows one of the six  $90 \times 90$  size LR frames obtained from a video sequence. Note that since this is a real data sequence captured by a video camera, it has some amount of input blur. To perform registration, it is necessary to know the motion parameters of the camera. Since these are not known a priori, these are estimated by the projective model in [14]. The results of applying the Delaunay triangulation method and the MLS technique are shown, respectively, in Figures 8(b) and 8(c). The resulting HR images obtained by both methods are seen to be comparable in visual quality. Also, the HR images from both methods are seen to contain a small amount of blur. This is to be expected since no post deblurring has been performed



Fig. 6. Reconstructed image by adaptive selection of scale and order. PSNR=22.50,  $M_{SVD}$ =0.06

on the HR image.

## V. CONCLUSIONS

In the continuous formulation of MLS applied to noise filtering and approximation of irregularly spaced data in the superresolution problem, an expression for filter bandwidth in terms of the order of polynomial approximation and the scale of the Gaussian weighting function is obtained. The discrete



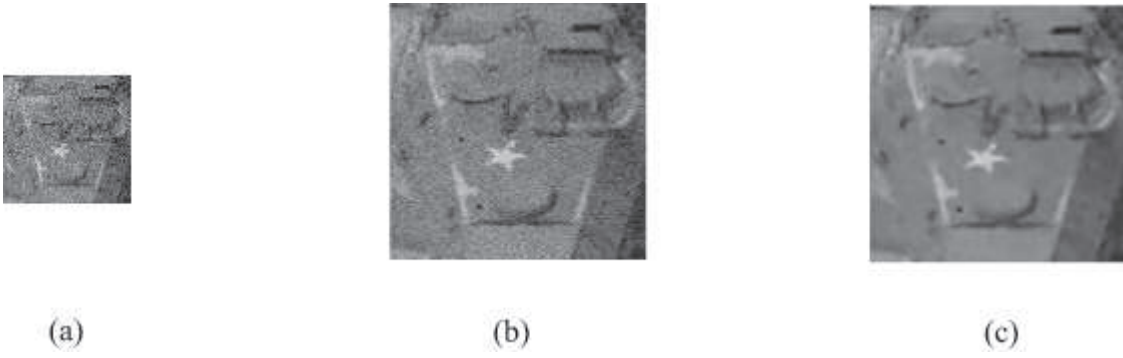


Fig. 7. Simulation results on tank sequence showing comparison between Delaunay Triangulation and MLS methods. (a) Sample LR frame of the tank sequence; (b) HR image using Delaunay Triangulation. PSNR=25.02,  $M_{SVD}$ =0.04; (c) HR image using MLS. PSNR=31.22,  $M_{SVD}$ =0.007.

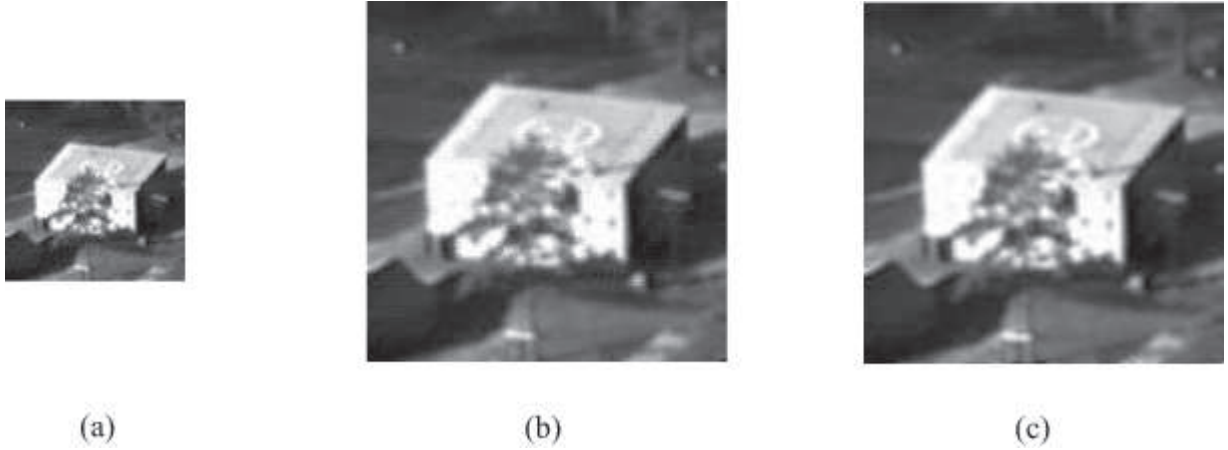


Fig. 8. Simulation results showing comparison between Delaunay Triangulation and MLS methods on a real-world data sequence. (a) Sample LR frame of the building sequence; (b) HR image using Delaunay Triangulation; (c) HR image using MLS.

implementation of MLS is performed on a sequence of LR images registered to form the grid of non-uniformly spaced data points. The MLS technique is then used adaptively to evaluate the values of the high-resolution image on a regularly spaced high-resolution grid. The parameters for adaptation in the local approximation are the scale and order. Noise in the output image increases with increasing order of approximation but reduces with increasing scale. On the other hand, the blur introduced reduces with increasing order but increases with increasing scale. For a given scale of the Gaussian weight function, the PSNR first increases with order of the image and then decreases again. This is because at low orders, degradation due to blur is higher than that due to noise, while at higher orders, the reverse happens. Between these two extremes, a tradeoff between the degrading effects of blur and noise produces a better image. This suggests that there is an optimal value of approximation order for a given scale. Similarly, there is an optimal value of scale for a given approximation order. Statistical and signal processing criteria for joint optimization of the two dependent parameters are applied to get optimal local tradeoff between noise filtration and reduction of blur introduced by the MLS process.

The availability of two parameters has the capability of producing greater robustness in numerical implementation than when only one parameter (threshold) is used to achieve optimal

tradeoff between noise filtering and blur removal [4]. Ideally, it would be desirable to introduce estimate of blur type and blur support parameters [7] [8, and references therein] into the superresolution process with not only noise filtering but also simultaneous deblurring.

One goal of future research is to study the approach advanced when input blur is present. Special attention may be required to obtain the irregularly sampled raster in Figure 1 in the presence of near field and medium field blurs for general camera motion. The second goal is to study the problem in the setting of multivariate orthogonal polynomials that are not product separable and by using weight functions that do not necessarily have circular support. For example, if the  $n$ -dimensional weight function is chosen to be the multivariate Gaussian given by

$$w(\mathbf{x}) \triangleq \frac{1}{(2\pi)^{n/2} \sigma_1 \dots \sigma_n} \exp \left\{ -\frac{1}{2} \left( \frac{x_1^2}{\sigma_1^2} + \dots + \frac{x_n^2}{\sigma_n^2} \right) \right\},$$

then a set of  $n$ -dimensional non-separable orthogonal Hermite polynomials can be found, as was proved by Grad in [24] for the case when  $\sigma_1 = \sigma_2 = \dots = \sigma_n = 1$ . The filter impulse response in the  $n$ -dimensional case can be obtained

by generalizing the expression in Eq. (30) as,

$$g(\mathbf{x}) = w(\mathbf{x}) \sum_{\mathbf{i}=0}^1 \left(-\frac{1}{4}\right)^{|\mathbf{i}|} \frac{1}{\mathbf{i}!} H_{2\mathbf{i}}^{[2\mathbf{i}]}(\mathbf{x}; \boldsymbol{\sigma}),$$

where,

$$\begin{aligned} \mathbf{x} &= [x_1 \ x_2 \ \dots \ x_n]^T, \mathbf{i} = [i_1 \ i_2 \ \dots \ i_n]^T, \\ |\mathbf{i}| &= i_1 + i_2 + \dots + i_n, \mathbf{i}! = i_1! i_2! \dots i_n!, \\ \sum_{\mathbf{i}=0}^1 &= \sum_{i_1=0}^{l_1} \sum_{i_2=0}^{l_2} \dots \sum_{i_n=0}^{l_n} \end{aligned}$$

and  $H_{2\mathbf{i}}^{[2\mathbf{i}]}(\mathbf{x}; \boldsymbol{\sigma})$  is the multivariate non-separable Hermite polynomial of total degree  $|\mathbf{i}|$  with the degree of  $x_j$  given by  $i_j$  for  $j = 1, 2, \dots, n$ . Adapting the shape of the weight function, and hence the neighborhood selected for each point, is shown to be a very effective technique in reducing blur [25]. However, the technique described in [25] does not adapt the order of approximation at each point. It is expected that by including such shape adaptivity with the scale and order adaptivity presented here, much better results can be obtained.

#### ACKNOWLEDGEMENT

The authors thank the three reviewers for their constructive suggestions and comments, which have been incorporated.

#### APPENDIX I

##### DERIVATION OF THE FILTER BANDWIDTH

A derivation of the bandwidth of the filter whose impulse response is given by Eq. (7) is presented here. For odd  $i$ ,  $H_i(x)$  is an odd function of  $x$  and hence  $\phi_i(0) = 0$ . As a result, only those terms in the summation in Eq. (7) need to be retained for which  $i$  is even. The summation in (7) can, therefore, be rewritten as

$$g(x) = \sum_{i=0}^l \frac{\phi_{2i}(0)\phi_{2i}(x)}{2^{2i}(2i)!} w(x), \quad (28)$$

where  $l = k/2$ , if  $k$  is even and  $l = (k-1)/2$  if  $k$  is odd. It can be shown that,

$$H_{2n}(0) = (-1)^n \frac{(2n)!}{n!}.$$

Using this, and the expressions for  $w(x)$  and  $\phi_i(x)$ , Eq. (28) simplifies to

$$g(x) = \sum_{i=0}^l \frac{(-1)^i \phi_{2i}(x)}{4^i i!} w(x) \quad (29)$$

$$= \frac{e^{-x^2/2\sigma^2}}{\sigma\sqrt{2\pi}} \sum_{i=0}^l \left(-\frac{1}{4}\right)^i \frac{1}{i!} H_{2i}\left(\frac{x}{\sigma\sqrt{2}}\right) \quad (30)$$

Interestingly, the preceding form for  $g(x)$  can be extracted from a result in [26], which is derived by considering the effect of the quantum free propagator on wave packets approximated by a linear combination of Hermite polynomials.

Replacing  $x$  by  $x/\sigma\sqrt{2}$  in Eq. (4) and using the result in (29) yields after simplification,

$$g(x) = \sum_{i=0}^l (\sigma^2)^i \frac{(-1)^i}{2^i i!} \frac{d^{2i}}{dx^{2i}} (w(x)).$$

The FT  $G(\omega)$  of  $g(x)$  is

$$G(\omega) = \sum_{i=0}^l \frac{(\sigma^2)^i (-1)^i (j\omega)^{2i}}{2^i i!} W(\omega) = W(\omega) \sum_{i=0}^l \frac{(\sigma^2 \omega^2)^i}{2^i i!}.$$

Therefore,

$$\int_{-\infty}^{\infty} |G(\omega)|^2 d\omega = \sum_{i=0}^l \sum_{j=0}^l \int_{-\infty}^{\infty} \frac{(\sigma^2 \omega^2)^{i+j}}{2^{i+j} i! j!} |W(\omega)|^2 d\omega. \quad (31)$$

The FT  $W(\omega)$  of  $w(x)$  is easily shown to be  $W(\omega) = e^{-\omega^2 \sigma^2/2}$ . Substituting this in Eq. (31),

$$\begin{aligned} \int_{-\infty}^{\infty} |G(\omega)|^2 d\omega &= \sum_{i=0}^l \sum_{j=0}^l \int_{-\infty}^{\infty} \frac{(\sigma^2 \omega^2)^{i+j}}{2^{i+j} i! j!} e^{-\omega^2 \sigma^2} d\omega \\ &= \sqrt{\frac{\pi}{\sigma^2}} \sum_{i=0}^l \sum_{j=0}^l \frac{\sigma^{2(i+j)} [2(i+j)]!}{2^{i+j} i! j! 4^{i+j} \sigma^{2(i+j)} (i+j)!} \\ &= \frac{\sqrt{\pi}}{\sigma} \sum_{i=0}^l \sum_{j=0}^l \frac{[2(i+j)]!}{8^{i+j} i! j! (i+j)!}, \end{aligned} \quad (32)$$

since

$$\int_{-\infty}^{\infty} \omega^{2n} e^{-\omega^2 \sigma^2} d\omega = \frac{1 \cdot 3 \dots (2n-1)}{2^n \sigma^{2n}} \sqrt{\frac{\pi}{\sigma^2}} = \frac{(2n)!}{\sigma^{2n} 4^n n!} \sqrt{\frac{\pi}{\sigma^2}}. \quad (33)$$

Similarly,

$$\int_{-\infty}^{\infty} \omega^2 |G(\omega)|^2 d\omega = \frac{\sqrt{\pi}}{2\sigma^3} \sum_{i=0}^l \sum_{j=0}^l \frac{(2i+2j+1)[2(i+j)]!}{8^{i+j} i! j! (i+j)!}. \quad (34)$$

Substituting Eq. (32) and Eq. (34) in the expression for bandwidth,

$$\Delta_\omega^2 = \frac{\int_{-\infty}^{\infty} \omega^2 |G(\omega)|^2 d\omega}{\int_{-\infty}^{\infty} |G(\omega)|^2 d\omega},$$

one gets,

$$\begin{aligned} \Delta_\omega^2 &= \frac{\frac{\sqrt{\pi}}{2\sigma^3} \sum_{i=0}^l \sum_{j=0}^l \frac{(2i+2j+1)[2(i+j)]!}{8^{i+j} i! j! (i+j)!}}{\frac{\sqrt{\pi}}{\sigma} \sum_{i=0}^l \sum_{j=0}^l \frac{[2(i+j)]!}{8^{i+j} i! j! (i+j)!}} \\ &= \frac{1}{2\sigma^2} \left[ 1 + \frac{2 \sum_{i=0}^l \sum_{j=0}^l \frac{i[2(i+j)]!}{8^{i+j} i! j! (i+j)!}}{\sum_{i=0}^l \sum_{j=0}^l \frac{[2(i+j)]!}{8^{i+j} i! j! (i+j)!}} \right. \\ &\quad \left. + \frac{2 \sum_{i=0}^l \sum_{j=0}^l \frac{j[2(i+j)]!}{8^{i+j} i! j! (i+j)!}}{\sum_{i=0}^l \sum_{j=0}^l \frac{[2(i+j)]!}{8^{i+j} i! j! (i+j)!}} \right] \\ &= \frac{1}{2\sigma^2} \left[ 1 + \frac{4 \sum_{i=0}^l \sum_{j=0}^l \frac{i[2(i+j)]!}{8^{i+j} i! j! (i+j)!}}{\sum_{i=0}^l \sum_{j=0}^l \frac{[2(i+j)]!}{8^{i+j} i! j! (i+j)!}} \right]. \end{aligned} \quad (35)$$

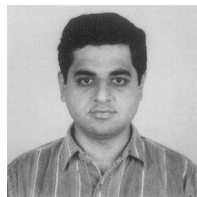
We believe that the formula for  $\Delta_{\omega}^2$  derived above is new and provides an analytical basis for guidelines in the parameter selection process.

## REFERENCES

- [1] S. P. Kim, N. K. Bose, and H. M. Valenzuela, "Recursive reconstruction of high resolution image from noisy undersampled multiframes," *IEEE Transactions on Acoustics, Speech and Signal Processing*, vol. 38, no. 6, pp. 1013–1027, 1990.
- [2] N. K. Bose, H. C. Kim, and H. M. Valenzuela, "Recursive total least squares algorithm for image reconstruction from noisy undersampled frames," *Multidimensional Systems and Signal Processing*, vol. 4, no. 3, pp. 253–268, 1993.
- [3] M. Elad, "On the origin of the bilateral filter and ways to improve it," *IEEE Transactions on Image Processing*, vol. 11, no. 10, pp. 1141–1151, 2002.
- [4] M. B. Chappalli and N. K. Bose, "Simultaneous noise filtering and super-resolution with second-generation wavelets," *IEEE Signal Processing Letters*, vol. 12, no. 11, pp. 772–775, November 2005.
- [5] A. Shnayderman, A. Gusev, and A. Eskicioglu, "A multidimensional image quality measure using singular value decomposition," *Proceedings of the SPIE Image Quality and System Performance Conference*, vol. 5294, pp. 82–92, 2003.
- [6] N. K. Bose and M. B. Chappalli, "A second generation wavelet framework for superresolution with noise filtering," *International J. on Imaging Science and Technology (Special Issue on High Resolution Image Reconstruction)*, vol. 14, no. 2, pp. 84–89, 2004.
- [7] S. Lertrattanapanich and N. K. Bose, "High resolution image formation from low resolution frames using Delaunay triangulation," *IEEE Transactions on Image Processing*, vol. 11, no. 12, pp. 1427–1441, 2002.
- [8] M. B. Chappalli and N. K. Bose, "Enhanced Biggs-Andrews asymmetric iterative blind deconvolution," *Multidimensional Systems and Signal Processing*, accepted for publication, 2005. [Online]. Available: [http://www.dsplab.ee.psu.edu/cgi-bin/publication\\_files/MULT189-KG.pdf](http://www.dsplab.ee.psu.edu/cgi-bin/publication_files/MULT189-KG.pdf)
- [9] M. Chiang and T. Boulton, "Efficient image warping and super-resolution," *Proceedings of the Third IEEE Workshop on Applications of Computer Vision*, pp. 56–61, 1996.
- [10] S. Farsiu, M. D. Robinson, M. Elad, and P. Milanfar, "Fast and robust multiframe super resolution," *IEEE Transactions on Image Processing*, vol. 13, no. 10, pp. 1327–1344, October 2004.
- [11] R. van den Boomgard and J. van de Weijer, "Least squares and robust estimation of local image structure," in *Scale-Space 2003, vol. 2695 of Lect. Notes. Comp. Sci.*, L. D. Griffin and M. Lillholm, Eds. Springer, 2003, pp. 237–254.
- [12] M. Fenn and G. Steidl, "Robust local approximation of scattered data," in *Geometric Properties from Incomplete Data*, R. Klette, R. Kozera, L. Noakes, and J. Weickert, Eds. Springer Series on Computational Imaging and Vision, September 2005, vol. 31.
- [13] H. Wendland, *Scattered Data Approximation*. Cambridge University Press, 2005.
- [14] S. Mann and R. W. Picard, "Video orbits of the projective group: a simple approach to featureless estimation of parameters," *IEEE Transactions on Image Processing*, vol. 6, no. 9, pp. 1281–1295, 1997.
- [15] *IEEE Signal Processing Magazine-Special Issue on Superresolution Image Reconstruction*, May 2003, vol. 20, no. 3.
- [16] N. K. Bose and P. Liang, *Neural Networks: Graphs and Algorithms*. McGraw-Hill Book Company, 1996.
- [17] C. Loader, *Local Regression and Likelihood*. Springer, 1999.
- [18] M. Stone, "Cross-validated choice of assessment of statistical predictions," *Journal of The Royal Statistical Society, Series B*, vol. 36, pp. 111–147, 1974.
- [19] C. Mallows, "Some comments on  $C_p$ ," *Technometrics*, vol. 15, pp. 661–675, 1973.
- [20] J. Fan, Q. Yao, and Z. Cai, "Adaptive varying-coefficient linear models," *Journal of The Royal Statistical Society, Series B*, vol. 65, no. 1, pp. 57–80, 2003.
- [21] W. S. Cleveland and C. L. Loader, "Smoothing by local regression: principles and methods," in *Statistical Theory and Computational Aspects of Smoothing*, W. Härdle and M. G. Schimek, Eds. Springer, New York, 1996, pp. 10–49.
- [22] H. Wendland, "Local polynomial reproduction and moving least squares approximation," *IMA Journal Of Numerical Analysis*, vol. 21, no. 1, pp. 285–300, 2001.
- [23] W. S. Cleveland and E. H. Grosse, "Computational methods for local regression," *Statistics and Computing*, vol. 1, pp. 47–62, 1991.
- [24] H. Grad, "Note on N-dimensional Hermite polynomials," *Commun. Pure Appl. Math.*, vol. 2, pp. 325–330, 1949.
- [25] T. Pham, L. van Vliet, and K. Schutte, "Robust fusion of irregularly sampled data using adaptive normalized convolution," *EURASIP Journal on Applied Signal Processing*, vol. To appear, 2005. [Online]. Available: [http://www.ph.tn.tudelft.nl/People/lucas/publications/2005/JoASP2005\\_TPLVKS.pdf](http://www.ph.tn.tudelft.nl/People/lucas/publications/2005/JoASP2005_TPLVKS.pdf)
- [26] D. K. Hoffman, N. Nayar, O. A. Sharafeddin, and D. J. Kouri, "Analytic banded approximation for the discretized free propagator," *Journal of Physical Chemistry*, vol. 95, no. 21, pp. 8299–8305, 1991.



**N. K. Bose** is the HRB-Systems Professor of Electrical Engineering at The Pennsylvania State University at University Park. From 1967 to 1986, he was at the University of Pittsburgh, Pittsburgh, where he became a Professor of Electrical Engineering and Professor of Mathematics. He received the B. Tech (Hons.), M.S., and Ph.D. degrees in electrical engineering from the Indian Institute of Technology (I.I.T.), Kharagpur, India, Cornell University, Ithaca, NY, and Syracuse University, Syracuse, NY, respectively. He is, since 1990, the founding editor-in-chief of the International Journal on Multidimensional Systems and Signal Processing and has served on the editorial boards of several other journals. He served as either a regular or visiting faculty for extended periods at several institutions, including the American University of Beirut, Lebanon, the University of Maryland, College Park, the University of California at Berkeley, Ruhr University (Germany) and Princeton University, Princeton. He was also invited for long term visits to LAAS at Toulouse, France, the Centre for Artificial Intelligence and Robotics in Bangalore, India, Tokyo Institute of Technology (1999–2000) and Akita Prefectural University in Japan (2005) to conduct research and give seminars. Professor Bose received several honors and awards, including, more recently, the Invitational Fellowship from the Japan Society for the Promotion of Science in 1999, the Alexander von Humboldt Research Award from Germany in 2000, and the Charles H. Fetter University Endowed Fellowship from 2001–2004. In 2005, Bose was cited for his pioneering contributions to multidimensional systems and signal processing and was among the "First 15" engineers to be inducted to the new "www.eng.pro" domain name. He was invited to serve as either the plenary keynote or opening speaker on many occasions. He is the author of several textbooks in multidimensional systems theory, digital filters, and artificial neural networks.



**Nileshe A. Ahuja** received the B.E. degree in electronics engineering from V.J.T.I., Mumbai University, Mumbai, India in 2001. From 2001 to 2003, he served as I.C. Design Engineer for Texas Instruments, Bangalore, India. In 2005, he received the M.S. degree in electrical engineering from the Pennsylvania State University, where he is currently a Ph.D. candidate in electrical engineering.